Inorganic Chemistry

pubs.acs.org/IC
Article

Twisted and Disconnected Chains: Flexible Linear Tetracuprous Arrays and a Decanuclear Cu^{I} Cluster as Blue- and Green/Yellow-Light Emitters

Janet Arras, Alvaro Calderón-Díaz, Sergei Lebedkin, Samer Gozem, Colin D. McMillen, Nattamai Bhuvanesh, and Michael Stollenz*

Cite This: *Inorg. Chem.* 2024, 63, 12943−12957

Read Online

ACCESS | Metrics & More | Article Recommendations | Supporting Information

ABSTRACT: Defined arrays of transition metal ions embedded in tailored polydentate ligand scaffolds allow for a systematic design of their physical properties. Such molecular strings of closed-shell transition metal centers are particularly interesting for Group 11 metal ions in the oxidation state +1 if they undergo metallophilic $d^{10}\cdots d^{10}$ contact interactions since these clusters are oftentimes efficient photoluminescence (PL) emitters. Copper is particularly attractive as a sustainable earth-abundant coinage metal source and because of the ability of several Cu^{I} complexes to serve as powerful thermally activated delayed fluorescence (TADF) emitters in molecular/organic light-emitting devices (OLEDs). Our combined synthetic, crystallographic, photophysical, and computational study describes a straight tetracuprous array possessing a centrally disconnected $Cu^{I}_2\cdots Cu^{I}_2$ chain and a continuous helically bent Cu^{I}_4 complex. This molecular helix undergoes a facile rearrangement in diethyl ether solution, yielding an unprecedented nanosized Cu^{I}_{10} cluster (2.9 × 2.0 nm) upon crystallization. All three clusters show either bright blue phosphorescence, TADF, or green/yellow multiband phosphorescence with quantum yields between 6.5 and 67%, which is persistent under hydrostatic pressure up to 30 kbar. Temperature-dependent PL investigations in combination with time-dependent density-functional theory (TD-DFT) calculations and void space analyses of the crystal packings complement a comprehensive correlation between the molecular structures and photoluminescence properties.

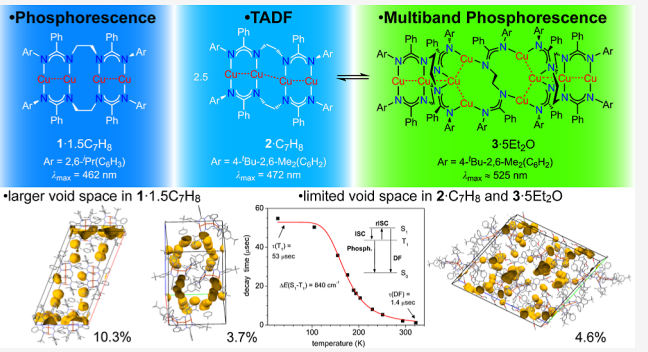

INTRODUCTION

Discrete linear arrangements of transition metal ions in designed ligand scaffolds have received tremendous attention within the past two decades.[1] These chain complexes are predominantly based on oligopyridyl amide ligands and have coined the term "extended metal atom chains" (EMACs)[2] which are highly popular because of their potential in serving as conducting molecular wires and as single molecule magnets (SMMs).[3] Nonconducting molecular strings of closed-shell transition metal centers are particularly interesting for Group 11 metal ions in the oxidation state +1 if they undergo $d^{10}\cdots d^{10}$ metallophilic contact interactions.[4] Such metallophilicity, which increases with increasing nuclear charge from Cu to Au due to increasing relativistic effects,[5−8] is oftentimes associated with intense luminescence properties of coinage metal clusters.[9] While mononuclear Ag^{I} and Au^{I} complexes without $d^{10}\cdots d^{10}$ contacts already serve as efficient triplet emitters, the relatively small spin−orbit parameter ξ of copper (856.99 cm^{-1}) in comparison to silver (1779.49 cm^{-1}) and gold (5104.20 cm^{-1}) usually impedes efficient phosphorescence of mononuclear Cu^{I} congeners (Scheme 1).[10]

However, it has been demonstrated by a series of mononuclear bis-phosphine/pyrrolide Group 11 metal complexes that Cu^{I} cations exhibit a significant d orbital contribution (through metal-to-ligand charge transfer, MLCT) to the lowest lying excited state. These Cu^{I} complexes have significantly larger intersystem crossing (ISC) rates and phosphorescence radiative decay rate constants (k_r^P) than their Ag^{I} and Au^{I} congeners.[11] In addition, copper is significantly cheaper than its higher silver or gold homologs and has also become highly attractive as energy-saving molecular/organic light-emitting device (OLED) components due to the potent thermally activated delayed fluorescence (TADF) behavior of several Cu^{I} complexes.[12,13] TADF is a powerful alternative to phosphorescence that is achieved by thermal population of the

Received: April 22, 2024
Revised: May 31, 2024
Accepted: June 5, 2024
Published: June 27, 2024

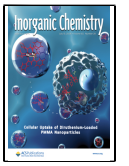

https://doi.org/10.1021/acs.inorgchem.4c01646
Inorg. Chem. 2024, 63, 12943−12957

Scheme 1. Simplified Mechanism for Phosphorescence and TADF in an OLED Emitting Component[a]

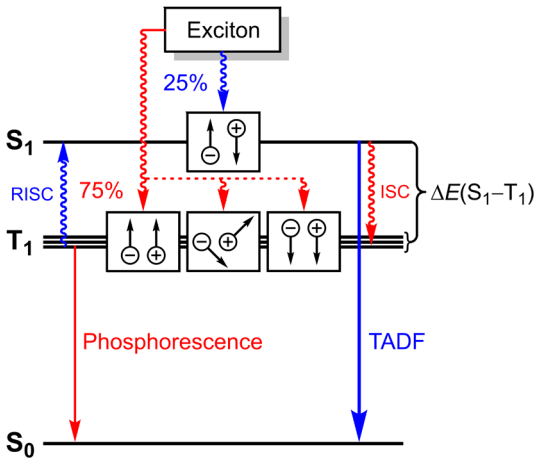

[a]Three triplet paths and one singlet path as well as (Phosphorescence) and RISC (TADF) are represented. Spin states and electron–hole recombinations are shown in boxes.

singlet S_1 state from energetically close populating triplet excitons through reverse intersystem crossing (RISC, Scheme 1). Cu^I complexes show fast RISC rates that allow for quantitative depopulation of the S_1 state and resulting monoexponential emission decays across a wide temperature range.

Despite these unquestionable advantages for applications in OLEDs,[9a−c,g−i] the number of linear multinuclear cuprous complexes with intramolecular $Cu^I\cdots Cu^I$ contacts is still limited.[4] This is because of the extreme weak nature of $d^{10}\cdots d^{10}$ cuprophilic interactions.[14] Except for rare examples of unsupported $Cu^I\cdots Cu^I$ contacts,[15] multinuclear Cu^I complexes with cuprophilic interactions usually require a tailored polydentate ligand framework to incorporate the Cu^I ions in close proximity (<2.8 Å, the sum of two Cu van der Waals radii)[16] to each other. A series of amidinate and guanidinate bridging ligands[17] has been found suitable for this purpose since corresponding binuclear Cu^I complexes originally served as examples for studies of closed-shell $d^{10}\cdots d^{10}$ interactions.[18] While binuclear cuprous complexes are well established, linear complex arrays with three or four Cu^I centers undergoing mutual $d^{10}\cdots d^{10}$ contact interactions are still rare in comparison to related Ag^I and Au^I clusters.[4,9h] There has been no example of such a linear pentanuclear Cu^I complex described yet. The longest discrete arrays of six Cu^I ions undergoing significant $d^{10}\cdots d^{10}$ interactions has been reported by Chen and Tsai et al. as well as by our group (complex **II**, Scheme 2).[19,20]

We became interested in flexible connected bis(amidines) for linear Cu^I complexes because they are extremely versatile ligands,[21,22] which have predominantly been employed in Groups 1–4,[23−26] 13,[27] and 14[28] coordination chemistry, together with related catalytic studies. Less, although recently growing interest in late transition metal complexes of bis(amidines) and bis(amidinates) is reflected by examples of Groups 8–11[29−32] that have also included multinuclear complex assemblies with more than two metal centers.[23c,31,32a] We chose alkylene-linked bis(amidinates) not only for designing multinuclear clusters but also for creating defined linear arrangements of Cu^I ions that are, due to the flexibility of the linker, substantially bent and therefore adopt structures of helices. The combination of multiple Cu^I centers undergoing cuprophilic interactions overcomes their small individual spin–orbit-coupling contributions and can facilitate phosphorescence-based emission of these systems.[33] Moreover, amidinates generally favor linear coordination spheres of the Cu^I centers and ensure rigid microenvironments in their interconnected binuclear $\{RC(NR')_2Cu_2(NR')_2CR\}$ compartments, which reduce large reorganization energies upon photoexcitation and also avoid Jahn–Teller distortions due to formal oxidation to d^9 electron configurations originating from typically observed MLCT events in luminescent Cu^I complexes.[34] Jahn–Teller distortions are known to increase nonradiative decay rates and further decrease intersystem crossing rates that are usually low in copper systems.

We have reported on a new ethylene-bridged bis(amidine) LH_2 that combines sterical protection through bulky mesityl substituents with a flexible linker. LH_2 cleanly reacts with mesitylcopper[35] to afford the bis(amidinate) complex $[Cu_2L]_n$ in 74% yield which crystallized simultaneously into **I** and **II** (from toluene/hexanes mixtures) or exclusively as **II** (from toluene/diethyl ether, Scheme 2).[19]

X-ray crystallography revealed complex **I** as a rare twisted linear array of four Cu^I ions that are embedded in a bis(amidinate) scaffold. Upon dimerization, the unique octanuclear cluster assembly **II** is formed that possesses a straight linear arrangement of six Cu^I centers with two additional bridging cuprous ions constituting a central pseudorhombic Cu^I_4 core. Both **I** and **II** are potent blue- (**I**: λ_{max} = 460 nm, as solvate **I**·C_7H_8) and green-light emitters (**II**: λ_{max} = 495 nm).

As subtle changes of the crystallization conditions (solvent polarity) have a fundamental impact on the selectivity of the formation of clusters **I** and **II**, we were curious about manipulations of the bis(amidinate) ligand backbone and its influence on the structures of $[LCu_2]_n$ complexes. In this report, we focus on two new bis(amidines) L^1H_2 and L^2H_2 that offer enhanced sterical protection at the ortho position through bulky isopropyl substituents (L^1H_2) and increased solubility by ^{t}Bu substituents in the 4-position of the terminal aryl groups (L^2H_2, Scheme 3). Upon clean conversion with mesitylcopper, L^1H_2 forms a straight linear Cu^I_4 cluster **1** in the crystalline state in which the tetracuprous chain is disconnected at the flexible diethylene bridge and thus represents a snapshot of the molecular dynamic process originally observed for **I**. By contrast, the corresponding bis(amidinate) complex **2** of L^2H_2 exhibits a tetranuclear Cu^I coil arrangement that resembles the structure of **I**, although **2** is significantly more twisted than **I**. Increasing the solvent polarity by using diethyl ether instead of toluene results in a rearrangement of **2** into the unprecedented Cu^I_{10} cluster **3** through dimerization that is accompanied by a formal insertion of a $[L^2Cu_2]$ fragment into the octanuclear Cu^I core assembly. Complexes **1**–**3** are efficient solid-state emitters in the visible

Scheme 2. Formation of Complexes I and II

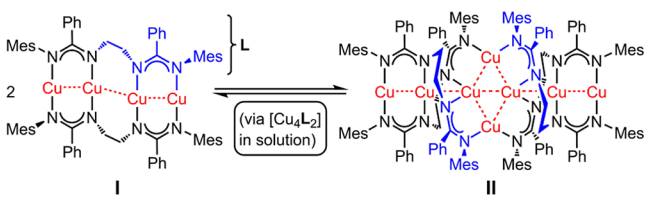

https://doi.org/10.1021/acs.inorgchem.4c01646
Inorg. Chem. 2024, 63, 12943−12957

Scheme 3. Synthesis of Ligands L^1H_2 and L^2H_2 and Their Single-Crystal XRD Molecular Structures[a]

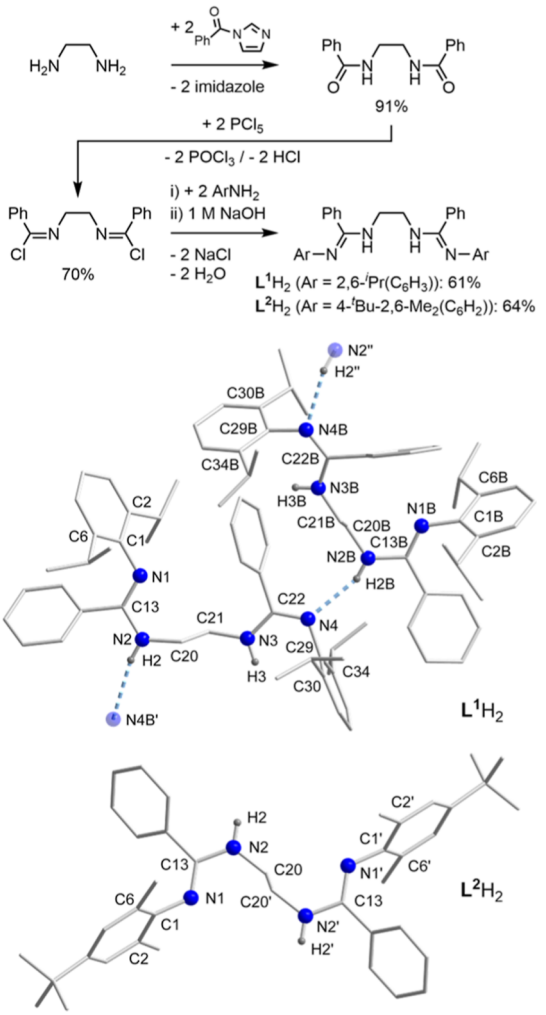

[a]Hydrogen atoms except for NH functionalities have been omitted for clarity. Symmetry operations used for L^1H_2 to generate equivalent atoms: (′) $x-1, y, z$ and (″) $x+1, y, z$. Symmetry operation used for L^2H_2 to generate equivalent atoms: (′) $-x+5/3, -y+4/3, -z+1/3$.

spectral range, with quantum yields as high as 67% (**2**). Their photoluminescence (PL) properties show not only similarities but also remarkable differences which are primarily attributed to their varying core structures in the solid state. The PL has been studied in the temperature range of 5−320 K, as well as at ambient temperature under high pressure in a diamond anvil cell. TD-DFT calculations for the gas phase reveal a correlation between the void spaces of the crystal lattices of the tetranuclear complexes and the different emission behavior of these two clusters.

RESULTS AND DISCUSSION

Synthesis, Structures, and Properties of L^1H_2 and L^2H_2. The synthesis of L^1H_2 and L^2H_2 was accomplished in three straightforward steps:[19,21] benzoylation of ethylenediamine, chlorination of the resulting bis(amide), and aminolysis of the bis(imidoyl chloride). Both ligands were isolated as colorless microcrystalline solids in reasonable yields (up to 64%, Scheme 3). The ^{1}H NMR spectra of L^1H_2 and L^2H_2 in C_6D_6 show broad resonance signals that suggest slow rotational motion of the bulky aromatic groups relative to the NMR time scale and proton exchange through tautomerization (Figures S36 and S40 in the Supporting Information). This is evidenced by a broad shoulder at δ = 3.27 ppm and an additional broad signal at δ = 7.81 ppm for L^1H_2 as well as additional broad signals at δ = 2.99 and 7.83 ppm for L^2H_2. These signals are indicative of *EE*/*EE*, *EZ*/*ZE*, and *ZZ*/*ZZ* C═N double bond as well as *syn*/*syn*, *syn*/*anti*, and *anti*/*anti* stereoisomers in solution that interconvert through tautomerization and single-bond rotation at the amidine moieties.[36] Since more polar solvents suppress the underlying prototopic exchange for this isomerization, additional signals in the DMSO-d_6 ^{1}H NMR spectra of both bis(amidines) disappear and also show decreased line broadening, although to a lesser extent for L^1H_2 than for L^2H_2. Consequently, also the ^{13}C NMR spectra of L^1H_2 and L^2H_2 in both solvents show broadened signals (Figures S37, S39, S41, and S43).

To examine the molecular structures in the solid state, single crystals of L^1H_2 and L^2H_2 suitable for X-ray structure analyses were both grown from diethyl ether solutions (Scheme 3). L^1H_2 was found to crystallize in the triclinic space group $P\bar{1}$ with two independent molecules in the asymmetric unit and four molecules in the unit cell (Figure S3 and Table S1). By contrast, ligand L^2H_2 crystallized in the trigonal space group $R\bar{3}$ with half of the molecule occupying the asymmetric unit and nine molecules being present in the unit cell (Figure S6 and Table S1). Increased steric bulk in the *ortho* positions of L^1H_2 in comparison to LH_2,[19] which occurs as an *EE*(*syn*/*syn*) isomer in the solid state, results in a preference for *Z*(*anti*) at one-half of the molecule of L^1H_2 whereas *E*(*syn*) is retained at the other half. The *Z*(*anti*) compartment of L^1H_2 features a considerably larger N═C−NH angle (125.58(17)°) than in *E*(*syn*) (L^1H_2: 119.47(17)°), which is consistent with the increased steric constraint for the latter. For this reason, the originally encapsulated bis(amidine) moiety of **L** unfolds in L^1H_2 and exposes the NH protons to hydrogen bonding. In consequence, an alternating polymeric chain of monomeric *EZ*(*syn*/*anti*) isomers of L^1H_2 that are linked through weak to moderately strong[37] intermolecular NH···N′ hydrogen bonds is observed (Scheme 3 and Figure S1). Very similar to the sterically crowded bis(amidine) LH_2,[19,21] ligand L^2H_2 also features the *EE*(*syn*/*syn*) isomeric configuration in the crystalline state (Scheme 3 and Figure S4). This results in considerable shielding of the bis(amidine) *N*-donor sites and prevents the NH groups from forming hydrogen bonds.

Consistently, the IR ν(N−H) stretching frequency of L^2H_2 is blue-shifted by 36−98 cm^{-1} relative to L^1H_2. As previously observed for a series of ethylene-linked bis(amidines),[21,22,23a,c] the NH protons of L^1H_2 and L^2H_2 are localized at the central −NH(CH$_2$)$_2$NH− diamine bridge. Its resulting N−C single bond character is reflected by large Δ_{CN} values[38] for both bis(amidines) (L^1H_2, *E*: 0.076 Å, *Z*: 0.060 Å; L^2H_2: 0.083 Å) that confirm only a low extent of delocalization within the −N═C−N− moieties.

Synthesis and Properties of $[L^1Cu_2]$ and $[L^2Cu_2]$. Formation and Solid-State Structures of $1{\cdot}1.5C_7H_8$, $2{\cdot}C_7H_8$, and $3{\cdot}5Et_2O$. Ligands L^1H_2 and L^2H_2 undergo a clean conversion with two equivalents of mesitylcopper in toluene at −35 °C and subsequent warming to room temperature to form the corresponding homoleptic Cu^I complexes of the stoichiometric composition ligand/Cu of 1:2 as almost

https://doi.org/10.1021/acs.inorgchem.4c01646
Inorg. Chem. 2024, 63, 12943−12957

colorless to pale yellow microcrystalline solids in good yields ($[L^1Cu_2]_n$: 69% and $[L^2Cu_2]_n$: 68%, Scheme 4).

Scheme 4. Synthesis of Complexes $[L^1Cu_2]$ and $[L^2Cu_2]$[a]

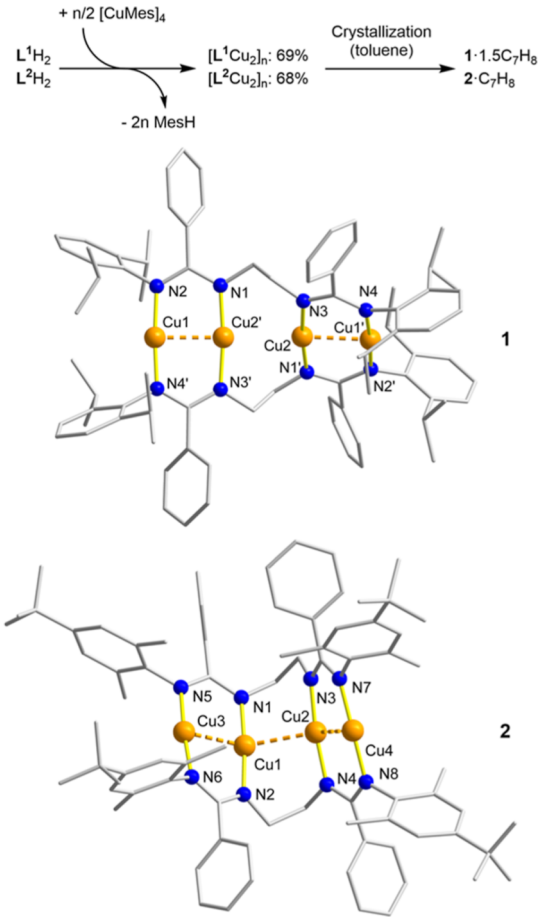

[a]Crystallization of $1\cdot1.5C_7H_8$ and $2\cdot C_7H_8$. Single-crystal XRD molecular structures of **1** and **2** (P (Δ) enantiomers). Toluene molecules and hydrogen atoms have been omitted for clarity. Symmetry operation used for **1** to generate equivalent atoms: $-x + 1, -y + 1, -z + 1$ and (′) $x, -y + 1, z + 1/2$.

Both Cu^I bis(amidinates) $[L^1Cu_2]_n$ and $[L^2Cu_2]_n$ are reasonably air-stable in the solid state and decompose at temperatures above 240 °C into a brown oil. Decomposition in solution (C_6D_6) was observed over the course of a few days at room temperature, even in an argon atmosphere.

The IR spectra of $[L^1Cu_2]_n$ and $[L^2Cu_2]_n$ indicate complex formation by the absence of ν(N−H) stretching frequencies. Both ^{1}H NMR and ^{13}C NMR spectra in C_6D_6 show one set of resonance signals of the ligand frameworks originating from $(L^1)^{2-}$ and $(L^2)^{2-}$, respectively, and therefore indicate the presence of one symmetrical complex species in solution (Figures S44−S47). All aliphatic and aromatic signals of the ^{1}H NMR spectra appear as narrow singlets or show well-resolved splitting patterns. Most characteristic for metal ion coordination are significant ^{13}C NMR downfield-shifts of the CH_2 signal by 14.8 ppm ($[L^1Cu_2]_n$) and 12.1 ppm ($[L^2Cu_2]_n$) as well as of the quaternary CN_2 amidinate resonance signals by 21.8 ppm ($[L^1Cu_2]_n$) and 20.0 ppm ($[L^2Cu_2]_n$). Although the molecular ion peak is not observed, ESI(+) mass spectrometry evidenced common characteristic fragments $[(L^{1,2}H_2)(L^{1,2}H)Cu_2]^+$ and $[(L^{1,2}H)_2Cu]^+$ at m/z = 1297.7 and 1235.7, respectively.

Crystallization of $[L^1Cu_2]_n$ and $[L^2Cu_2]_n$ afforded the formation of complexes $1\cdot1.5C_7H_8$ and $2\cdot C_7H_8$ (Scheme 4). Single crystals suitable for XRD analyses were obtained from slowly evaporating ($1\cdot1.5C_7H_8$) or saturated toluene solutions ($2\cdot C_7H_8$) at room temperature or −35 °C, respectively. Under exposure to UV light, both crystalline materials exhibit bright blue emissions with maxima at ≈470 nm. Complex **1** crystallized in the monoclinic space group $C2/c$ and half of one molecule of **1** was found in the asymmetric unit to translate into four molecules in the unit cell, together with overall six cocrystallizing toluene molecules (Figure S9 and Table S2). Complex **2** formed a solvate $2\cdot C_7H_8$ in the monoclinic space group $P2_1/n$ with one molecule of **2** and toluene each being present in the asymmetric unit (four molecules were found in the unit cell, Figure S13 and Table S2).

Complex **1** consists of two sets of double-μ-1,3-amidinate-bridged Cu^I_2 segments that are terminally interconnected by two flexible ethylene linkers (Scheme 4 and Figure S7). Similar to **I**,[19] the structural motif of these eight-membered dicopper(I)-diamidinate units resembles the one of well-established binuclear Cu^I diamidinate complexes.[18]

The peripheral Cu^I centers adopt distorted linear or T-shaped coordination geometries, the latter if $d^{10}\cdots d^{10}$ contacts are considered as chemical bonds, as indicated by the N4′−Cu1−N2/N4−Cu1′−N2′ angles of 175.67(9)°. This deviation from linearity is more distinct for the inner cuprous ions (N3′−Cu2′−N1: 173.69(9)°). The terminal $(CN_2)Cu_2$ rings of **1** exhibit a substantial twist (N4′−Cu1−Cu2′−N1: −171.4(1)°) which is typical of dicopper-diamidinate complexes[18] and was previously observed for complex **I** [N1−Cu1−Cu2′−N3′: 168.169(2)°].[19] In contrast to the helically bent chain of four Cu^I ions in **I** [$Cu_{(out)}$−$Cu_{(in)}$−$Cu_{(in)}$′: 139.79(3)°], complex **1** shows an almost ideal linear array of four Cu^I ions as reflected by an $Cu_{(out)}$−$Cu_{(in)}$−$Cu_{(in)}$′ angle of 176.400(15)°, although the helical bending of the dibis(amidinate) ligand framework is even more pronounced in **1** than in **I** (Figure S19). This is obvious by the torsion angles of the *N*-donor atoms defining the central 10-membered −{μ-($Cu_{(in)}$)(N−CH_2−CH_2−N)$_2$($Cu_{(in)}$)}− rings in both complexes (P (Δ) enantiomers, **1**: N3′−N1−N3−N1′, 40.31(6)°; **I**: N3−N2′−N3′−N2, −28.852(1)°).[19,39] In contrast to **I**, the Cu^I_4 chain in **1** undergoes a formal relaxation that is accompanied by a disconnection of the central $Cu_{(in)}\cdots Cu_{(in)}$′ contact, as evidenced by an intermetallic distance of 2.8702(6) Å, which is clearly longer than the sum of two copper van der Waals radii of 2.8 Å.[16] The separated dicopper(I) units in **1** reveal slightly longer $Cu^I\cdots Cu^I$ distances (2.4771(4) Å) than in **I** and **2** (2.4398(9)−2.4640(13) Å). Overall, the centrally disconnected ($Cu_{(out)}\cdots Cu_{(in)}$)($Cu_{(in)}$′$\cdots Cu_{(out)}$′) chain in **1** represents a remarkable snapshot of the molecular dynamic process previously observed in solution for **I**.

The molecular structure of **2** is very similar to **I** and consists of two ethylene-interlinked sets of double-μ-1,3-amidinate-bridged dicopper(I) segments with short $Cu^I\cdots Cu^I$ distances (2.4398(9) Å and 2.4579(9) Å) that are indicative of significant $d^{10}\cdots d^{10}$ contacts (Scheme 4 and Figure S11). The two central Cu^I ions undergo cuprophilic interactions as well, although to a lower extent ($Cu^I\cdots Cu^I$: 2.6464(9) Å), but they are more significant if this distance is compared to the inner $Cu^I\cdots Cu^I$ separation of **I** (2.6796(17) Å). In consequence, a

https://doi.org/10.1021/acs.inorgchem.4c01646
Inorg. Chem. 2024, 63, 12943−12957

continuous array of four cuprous ions with intermetallic contact distances is observed. If these contacts are considered as chemical bonds, then the central Cu^I centers adopt distorted-seesaw coordination geometries, with smaller equatorial $Cu_{(out)}-Cu_{(in)}-Cu_{(in)}'$ angles (131.37(3)° and 137.41(4)°) than in **I** (139.79(3)°), thus indicating a more twisted Cu^I_4 chain in **2** (Figure S19).

We noticed that $[\mathbf{L}^2Cu_2]_n$ is substantially more soluble in common organic solvents (THF, toluene, C_6D_6) than $[\mathbf{L}^1Cu_2]_n$. It is even possible to obtain clear solutions of $[\mathbf{L}^2Cu_2]_n$ in diethyl ether. Upon slow evaporation at room temperature, pale yellow, almost colorless single crystals of a new complex **3** were obtained that emit green-yellowish light ($\lambda_{max(295K)} \approx 525$ nm) under UV light exposure (Scheme 5).

Scheme 5. Formation of Complex 3·5Et$_2$O upon Crystallization from Diethyl Ether[a]

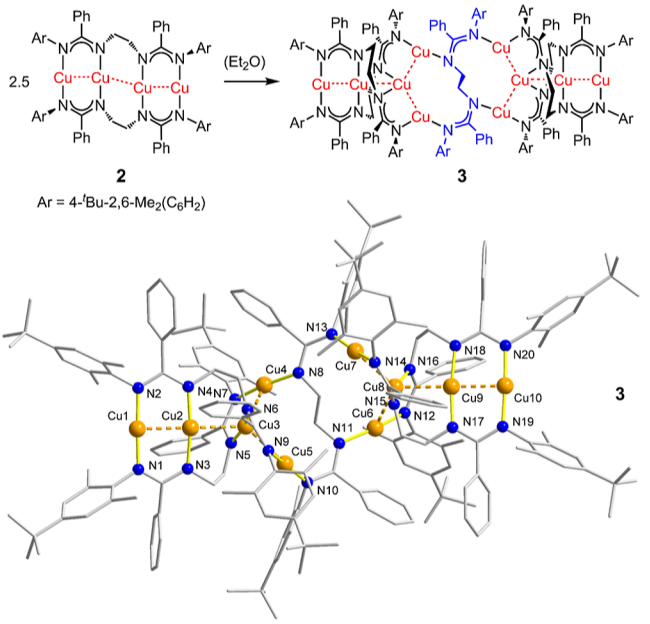

[a]Single-crystal XRD molecular structure of **3** (*P* (Δ) enantiomer). Diethyl ether molecules and hydrogen atoms have been omitted for clarity. Symmetry operation used to generate equivalent atoms: $-x + 1, -y + 1, -z$.

An X-ray crystallographic structure determination shows that **3** crystallized in space group $P\bar{1}$ with two independent molecular units in the asymmetric unit and four molecules in the unit cell, together with overall 20 diethyl ether solvent molecules (Figure S17). The structure of **3**·5Et$_2$O is represented by a nanoscaled molecular aggregate with an approximate length of 29 Å and a height of 20 Å consisting of two Y-shaped pentanuclear Cu^I clusters $[\mathbf{L}_2{}^2Cu_5]^+$ that are interconnected by a flexible bis(amidinate) bridge $(\mathbf{L}^2)^{2-}$ (Scheme 5, Figure S15, Table S2).

A density functional theory (DFT, PBE0) gas-phase investigation revealed an overall exothermic ($\Delta H = -15.46$ kcal·mol^{-1}) but endergonic ($\Delta G = 13.94$ kcal·mol^{-1}) aggregation process for $2.5 \times \mathbf{2} \rightarrow \mathbf{3}$. This is consistent with our previous observation for the dimerization of **I** to **II**, in which also a negative formation enthalpy ($\Delta H = -4.76$ kcal·mol^{-1}) and positive free energy change ($\Delta G = 17.88$ kcal·mol^{-1}) was found for the gas phase.[19] The aggregation energy is expected to be small for both transformations because the two cluster pairs (**2** and **3** as well as **I** and **II**, respectively) crystallize at the same temperature conditions and can even coexist through simultaneous formation (**I** and **II**). The PBE0 calculations were performed in the gas phase and therefore overestimate the entropy contribution to the free energy for the solid state. Generally, DFT underestimates the stabilization of the larger clusters **3** and **II** by additional van der Waals interactions which have been found as significant contributions in related binuclear bis(amidine) coinage complexes.[32] Taking these factors into account, the calculated free energy of aggregation for **3** is within reason for its formation in the crystalline state.

The decanuclear Cu^I cluster **3** is likely formed from an intermediate dimeric Cu^I_8 assembly similar to **II** (Scheme 2) that subsequently incorporates a $[\mathbf{L}^2Cu_2]$ fragment by formal insertion into the original central pseudorhombic Cu^I_4 core. Two molecular units of $[\mathbf{L}_2{}^2Cu_4]$ open one terminal $(CN_2)Cu_2$ ring to aggregate with one additional Cu^I ion each that is formally inserted into one Cu−N bond of each of the two diamidinate-dicuprous segments. This rearrangement of two formerly twisted $[\mathbf{L}_2{}^2Cu_4]$ parent complexes relieves strain on the helically bent Cu^I_4 chain to yield a straight linear arrangement of three Cu^I ions within the two Y-shaped Cu^I_5 cluster compartments (Cu1−Cu2−Cu3: 176.64(3)°; Cu10−Cu9−Cu8: 177.37(3)°). Similar to complex **II**, the helical twist of the bis(amidinate) ligands is thereby enforced, as reflected by the significantly larger torsion angles within the double-bridge $\{-N-CH_2-CH_2-N-\}_2$ moieties of **3** in comparison to **2** (**3**: N4−N3−N5−N6: 45.60(9)°;[39] N15−N16−N18−N17: 45.07(9)°;[39] and **2**: N1−N2−N4−N3: 27.2(1)°).[19] To ensure balancing the charge and coordinative saturation of the two cuprous ions, an additional $(\mathbf{L}^2)^{2-}$ bis(amidinate) acts as a bridging ligand for a total of four Cu^I centers. While the terminal cuprous centers of this central $[\mathbf{L}^2Cu_4]^{2+}$ unit are coordinated in the usual *E* fashion known from several dicopper-diamidinate complexes,[18] the inner Cu^I centers adopt a unique side-on coordination originating from a *syn*/*syn* conformational orientation of the bis(amidinate) ligand as it is observed in the solid-state structure of $\mathbf{L}^2H_2$ (*vide supra*). All five cuprous ions in each compartment undergo $d^{10}\cdots d^{10}$ contact interactions, as indicated by intermetallic distances ranging between 2.4783(7) and 2.6664(8) Å. If these interactions are considered as chemical bonds, then the individual Cu^I centers exhibit T-shaped, square-planar, or trigonal-bipyramidal[40] coordination geometries, respectively. Similar to the Cu^I_8 cluster **II**, the peripheral tethered dicopper-diamidinate units show elongated $Cu^I\cdots Cu^I$ separations (Cu2···Cu3: 2.6077(7) Å; Cu9···Cu8: 2.6437(7) Å) to the neighbored Cu3/Cu8 centers in comparison with the intra-segmental Cu1(Cu10)···Cu2(Cu9) distances (2.4783(7) Å and 2.4874(7) Å, respectively). However, the corresponding distances to the central Cu^I_4 rhomb in **II** are significantly longer by about 0.06−0.09 Å.

All three complexes **1**−**3** crystallized as racemic mixtures of *P* (Δ) and *M* (Λ) isomers (Figures S9, S13, and S17). Since the arrays of Cu^I ions in **1** and **3** are strictly linear, the helicity of these complexes is exclusively determined by the bis(amidinate) ligand framework. This is in striking contrast to complex **2** in which the tetranuclear Cu^I_4 chain is also helically bent.

DFT Calculations Related to the Structures of 1−3. The ground-state optimized structures of **1** and **2** for the gas phase undergo notable geometrical changes relative to the X-

https://doi.org/10.1021/acs.inorgchem.4c01646
Inorg. Chem. 2024, 63, 12943−12957

ray structures that predominantly originate from the common flexible $-\{\mu\text{-}(Cu_{(in)})(N-CH_2-CH_2-N)_2(Cu_{(in)})\}-$ rings (Figures S20 and S21). This is most obviously indicated by a bending tetracuprous chain in **1** upon computational geometry optimization, resulting in a deviation of 17.0−17.1° from approximate linearity of the crystal structure analysis (Table S3). This structural change is accompanied by a significant decrease of the central Cu2···Cu2′ distance by 0.225 Å, thus establishing a contact interaction of the originally disconnected $(Cu^I_{(out)}\cdot\cdot Cu^I_{(in)})(Cu^I_{(in)}{}'\cdots Cu^I_{(out)}{}')$ chain. The geometry-optimized computational structure of **2** shows a tendency of decreased bending of the Cu^I_4 chain, as reflected by an increase of the Cu3−Cu1−Cu2 and Cu4−Cu2−Cu1 angles of 4.6 and 10.6°, respectively (Table S4). The existing central Cu1···Cu2 cuprophilic interaction remains intact (2.664 Å). This trend is consistent with previous DFT calculations on **I**, which suggests that both complexes **I** and **2** undergo crystal packing effects that support the helical bend of the common Cu^I_4 chain.[19] Overall, the structural changes of the Cu^I_4 chain through computational geometry optimization are more pronounced in complex **1** than in **2**. In consequence, both complex molecules become more similar in terms of the central $Cu^I\cdots Cu^I$ contact and helical bending in the gas phase when compared to the crystalline state. In contrast, the more rigid ligand scaffold of **3** allows for a reasonable agreement between the crystal structure analysis and the gas-phase geometry-optimized structure (Figure S22).

The connected chain character of the computational structure of **1** is confirmed by its orbital analysis (Figures 1 and S23−S25). Selected molecular orbitals clearly show delocalization of the σ bonding orbitals of the Cu atoms (MO 333 of **1**) as well as π bonding within the Cu^I_4 chain (MO 339 of **2**, see also Figures S26−S28). For the decanuclear cluster **3**, electron density is mainly observed in the linear tricuprous segments (Figures 1 and S29−S31). While this delocalization does not necessarily mean that there is a net bonding character between the Cu atoms, these occupied orbitals, in addition to $Cu^I\cdots Cu^I$ contacts shorter than the sum of two copper van der Waals radii, indicate the existence of weak cuprophilic interactions.

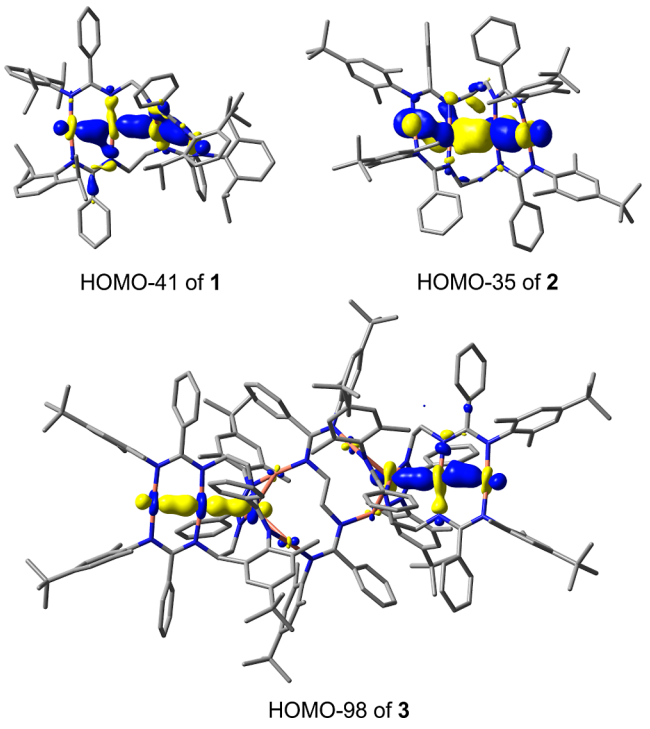

Figure 1. Isodensity plots of selected molecular orbitals of **1**−**3** showing electron delocalization across the Cu centers (isovalues = 0.04 au for **1** and **3**, and 0.02 au for **2**).

Photoluminescence Properties of 1−3 and Their Solvates. Figure 2 compares PL emission and excitation

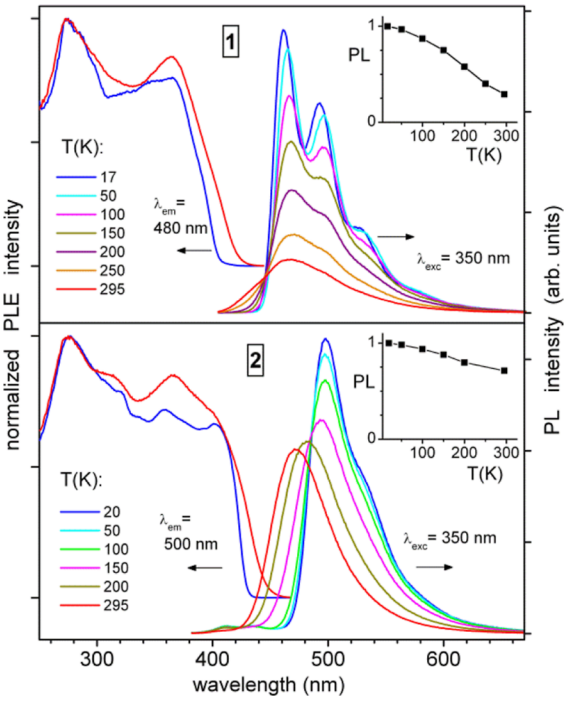

Figure 2. Temperature-dependent photoluminescence emission (PL) and excitation (PLE) spectra of polycrystalline complexes $\mathbf{1}\cdot 1.5C_7H_8$ and $\mathbf{2}\cdot C_7H_8$. The inserts show an integral PL intensity (normalized to unity) as a function of temperature.

(PLE) spectra of the tetranuclear complexes $\mathbf{1}\cdot 1.5C_7H_8$ and $\mathbf{2}\cdot C_7H_8$ in the temperature range of 17−295 K. The PLE onset at ≈430−450 nm at ambient temperature corresponds well to the pale yellow color of the crystalline materials. Blue/blue-green emission peaks were found at 467/461 and 472/495 nm for $\mathbf{1}\cdot 1.5C_7H_8$ and $\mathbf{2}\cdot C_7H_8$, respectively, when measured at 295/20 K. Complex $\mathbf{1}\cdot 1.5C_7H_8$ features a quantum yield of 6.5% at 295 K ($\mathbf{1}\cdot C_7H_8$: 17%) and was determined using an integrating sphere (excitation at 400 nm). A distinct feature of the low-temperature emission of $\mathbf{1}\cdot 1.5C_7H_8$ is a pronounced vibronic progression with a characteristic frequency of ∼1400 cm^{-1}, likely relating to a vibration of the amidinate bridge. A similar feature is also observed for $\mathbf{2}\cdot C_7H_8$, but only as a shoulder on the emission curve. The PL of $\mathbf{1}\cdot 1.5C_7H_8$ and of $\mathbf{2}\cdot C_7H_8$ at low temperatures is phosphorescence as indicated by a long (tens of μs) emission decay under pulsed laser excitation (Figures S48 and S49). The PL decay of $\mathbf{1}\cdot 1.5C_7H_8$ only moderately accelerates at 295 versus 18 K, roughly correlating with the decrease in PL intensity. In contrast, $\mathbf{2}\cdot C_7H_8$ shows a significant variation of the decay time, τ, following a temperature dependence characteristic for thermally activated delayed fluorescence (TADF), i.e., emission from the singlet S_1 state thermally populated from the low-lying, energetically close triplet T_1 state. Accordingly, the T_1 phosphorescence of

https://doi.org/10.1021/acs.inorgchem.4c01646
Inorg. Chem. 2024, 63, 12943−12957

2·C_7H_8 observed below ∼120 K (average τ of 53 μs) transforms to TADF by raising the temperature. The latter is dominating above 200 K, resulting in the effective PL lifetime of 1.4 μs at 325 K. By applying the simple TADF model of the thermally equilibrated S_1 and T_1 states,[13a−c] the energy separation between these states, $\Delta E(S_1-T_1)$, and intrinsic S_1 lifetime can be estimated as 840 cm^{-1} and 16 ns (Figure S49). The TADF mechanism also agrees with the emission blueshift (∼1000 cm^{-1}) between 295 and <100 K.

Remarkably, after washing with hexanes and vacuum drying, the PL efficiencies of **1** and **2** at 295 K soar to 58 and 67% (λ_{exc} = 400 nm), respectively. This can be attributed to removal of cocrystallized solvent molecules (C_7H_8) which might contribute to nonradiative electronic relaxation. In comparison to **2**·C_7H_8, the emission of **2** shows a moderate redshift ($\lambda_{max(295K)}$ = 495 nm, Figure S50). Due to such a high quantum yield, the perceived color of **2** in daylight turns to green, similar to "neon colors" known for highly efficient fluorophors.[41] The parameters of the TADF-characteristic emission decay, in particular the estimate of $\Delta E(S_1-T_1)$, remain, however, standing (Figure S51).

The decanuclear cluster complex **3**·5Et_2O demonstrates similar solid-state PLE spectra as **1** and **2** (with the onset at ≈430 nm at 295 K), but green-yellowish phosphorescence which is spectrally very broad, tailing up to about 750 nm (Figure 3). Its quantum efficiency was determined as 12.5% at

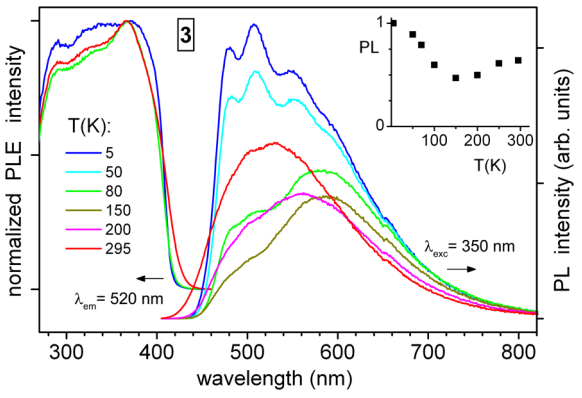

Figure 3. Temperature-dependent photoluminescence emission (PL) and excitation (PLE) spectra of polycrystalline complex **3**·5Et_2O, excited. The inset shows an integral PL intensity (normalized to unity) as a function of temperature.

ambient temperature (λ_{exc} = 400 nm). The emission of **3**·5Et_2O follows a rather unusual thermochromism pattern: its maximum red-shifts to ≈590 nm (and the emission color changes to orange) by cooling down to about 150 K, and blue-shifts back to 506 nm (the maximum of a moderately pronounced vibronic pattern similar to that in **1**) by further cooling below 50 K.

This change is accompanied by a specific "U-shaped" variation of the integral PL intensity: this first decreases by cooling down to 150 K, and then again increases at lower temperatures (Figure 3). The mechanistic details behind such behavior are presently not clear. Tentatively, we attribute this to complicated multichannel electronic relaxation in **3**·5Et_2O, likely related to the large, double-unit core structure. Such picture appears to be supported by complicated PL kinetics observed for this cluster compound below ∼200 K. Especially in the intermediate temperature range of 100−200 K, the PL decay is clearly nonexponential and dependent on the emission wavelength (Figure S52).

Additional experimental data on the relation between a structure and photophysical properties were delivered by high pressure measurements in a diamond anvil cell up to 30 kbar (the maximum level probed in this work). Within this pressure range, **1**, **2** (chosen as the most bright emitter), and **3**·5Et_2O display significant redshifts of both excitation and emission spectra, accompanied by acceleration of the PL decay (Figures S53−S55). Such shifts can be expected for the excited states of MLCT character, extending over a molecular framework (see DFT and TD-DFT Calculations Related to the Photophysical Properties of 1−3 below). Specifically, the PLE onsets approximately linearly shift up to 50−70 nm under 25−30 kbar pressure, corresponding to energy shifts of −(10−15) meV/kbar. The effect on the phosphorescence corresponds to a shift of about −10 meV/kbar for **1** and **2**, and −4 meV/kbar for **3**·5Et_2O. Somewhat unexpectedly, we found for complexes **1**, **2**, and **3**·5Et_2O a high resilience to (quasi)hydrostatic pressure (up to 30 kbar). After pressure release, the PL spectra, emission intensity, and decay almost recover for **1**, and practically completely recover for **2** and **3**·5Et_2O. The higher pressure resilience of the latter most likely correlate with the less void space in their crystal structures (see above). The decanuclear cluster appears thereby to be the most pressure-resilient structure. Regardless of the spectral shifts, application of high pressure only moderately reduces its emission intensity (Figure S55). An interesting pressure effect is also observed regarding the TADF emission of **2**. Its redshift notably increases and intensity decreases above ∼15 kbar (Figure S54). Even more remarkable are the fast PL decay and the appearance of a prompt fluorescence component in decay traces above ∼15 kbar. These observations suggest that TADF is not sustained in **2** under high pressure (but recovers after pressure release).

DFT and TD-DFT Calculations Related to the Photophysical Properties of 1−3. Inspection of the frontier orbitals of **1**−**3** reveals the charge-transfer character of the lowest excited states of all three complexes, with major contributions from MLCT (Figure 4). The HOMOs of all three complexes are largely derived from the Cu^I 3d atomic orbitals but also contain contributions from the amidinate *N*-donor atoms. Very little electron density is observed on the terminal aromatic substituents of **1**−**3**. The LUMOs are predominantly located on the phenyl groups and the sp^2-hybridized amidinate carbon atoms. TD-DFT and natural transition orbital (NTO) calculations (Figure S32) indicate that the experimentally observed $S_1 \leftrightarrow S_0$ and $T_1 \leftrightarrow S_0$ transitions correlate with leading electron/hole NTOs that describe the excitation character with a weight of over 84% for **1** and **2**, and 20.3−97.5% for **3**. NTOs more compactly represent the character of the excitation than the canonical molecular orbitals depicted in Figure 4. The NTO pairs of both complexes **1** and **2** clearly show electron density at the central $Cu^I_{(in)}\cdots Cu^I_{(in)}{}'$ contact (Figure S32) that is apparently induced upon closure of the Cu^I_4 chain in the case of complex **1**. This observation is further supported by a significant decrease of the central $Cu^I_{(in)}\cdots Cu^I_{(in)}{}'$ contact distances in **1** and **2** upon excitation to the S_1 and T_1 states. By contrast, complex **3** exhibits substantial ligand-to-ligand charge transfer (LLCT) for T_1. On the basis of these computational results, the lowest singlet and triplet excited states of **1**−**3** are assigned

https://doi.org/10.1021/acs.inorgchem.4c01646
Inorg. Chem. 2024, 63, 12943−12957

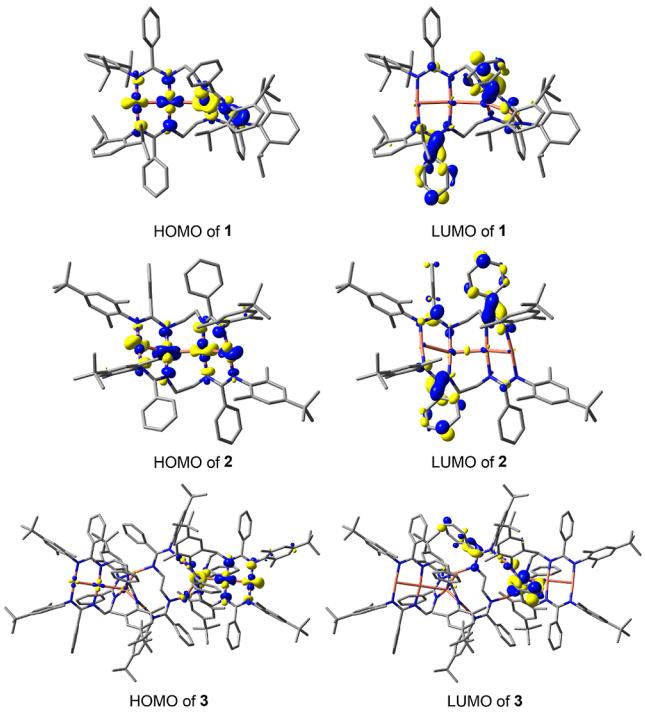

Figure 4. Isodensity plots of the highest occupied molecular orbitals (HOMOs) and lowest unoccupied molecular orbitals (LUMOs) of **1**−**3** (iso value = 0.04 au).

as S_1 = ^{1}MLCT (dπ*) T_1 = ^{3}MLCT, (dπ*) states. The T_1 state of **3** is dominated by LLCT (pπ*) transitions.

The calculated S_1−T_1 adiabatic energy separations of **1** and **2** are very similar for the gas phase (**1**: 2071 cm^{-1} and **2**: 2180 cm^{-1}), although each of them has a different ground-state geometry (Figure S33). Nevertheless, these geometry-optimized structures are more similar to each other than in the solid state (*vide infra*). The low-lying excited states are ordered in a similar way with differences in absolute energies no larger than 0.03 eV. This suggests that complexes **1** and **2** would be expected to have very similar photophysical properties in the gas phase. These computational results appear to be in contradiction to the experimental data because they show that only **2** is capable of thermally accessing its singlet excited state. However, the molecular structures of the two complexes are significantly different in the crystalline state. The structural changes of their Cu^I_4 chains through computational geometry optimization for the gas phase are more pronounced in complex **1** than in **2** (*vide supra*). On the other hand, there are smaller structural changes for **1** observed upon photoexcitation in the gas phase (Figures S34 and S35 and Tables S3 and S4). In the S_1 structure of **1**, the $Cu_{(out)}$−$Cu_{(in)}$−$Cu_{(in)}'$ angles are increased by 12.6 and 14.3°, while **2** shows a more substantial increase of 13.1 and 21.4° in the first excited singlet state. The effect is an induced relaxation toward linearity in both structures. In the T_1 state, complex **1** adopts a more linear structure in one half of the molecular structure in comparison to the S_0 ground state, as indicated by an increase of the corresponding $Cu_{(out)}$−$Cu_{(in)}$−$Cu_{(in)}'$ angle of 9.7° (to 169.1°). The clearly more bent ground-state structure of complex **2** becomes distinctly more linear in the T_1 state (by +20.9° relative to S_0), effectively showing the same degree of linearity as in **1** ($Cu_{(out)}$−$Cu_{(in)}$−$Cu_{(in)}'$: 168.9°). Due to Jahn−Teller distortion, the second half of both molecular structures of **1** and **2** is evidently more distorted (the $Cu_{(out)}$−$Cu_{(in)}$−$Cu_{(in)}'$ angle for **1** is 149.4 and 133.6° for **2**). The central $Cu_{(in)}$···$Cu_{(in)}'$ distances in **1** and **2** become smaller in the S_1 and T_1 states and they are also very similar to each other (for S_1, **1**: 2.446 Å and **2**: 2.488 Å; for T_1, **1**: 2.561 Å and **2**: 2.593 Å, Tables S3 and S4).

Overall, upon photoexcitation, gas phase calculations indicate that complex **1** undergoes fewer structural changes than **2**, from a slightly bent ground-state structure to an almost linear arrangement in the S_1 state. The S_1 structure of **2** is formed by larger structural rearrangements than in **1** and resembles the S_1 structure of **1**. For the first triplet excited state, both structures are even more similar to each other. In the gas phase, such structural rearrangements are relatively unconstrained, which leads to similar computed vertical and adiabatic $\Delta E(S_1-T_1)$ values for **1** and **2** in the gas phase calculations. However, in the solid state, intermolecular interactions place steric constraints that prevent the molecules from undergoing large-scale motions, resulting in more linear structures of the S_1 and T_1 states of **1** and **2**. An analysis of the available void space of the crystal packings of **1**·1.5C_7H_8, **2**·C_7H_8, and **3**·5Et_2O, using spherical probes (radius: 1.2 Å), confirms that **1**·1.5C_7H_8 offers appreciably more void space (10.3%) than **2**·C_7H_8 (3.7%, Figures S10 and S14).[42] This is consistent with the hypothesis that molecular motion in the crystal structure of **2**·C_7H_8 is more restricted than in **1**·1.5C_7H_8. For this reason, there is strong evidence that the origin of the different photophysical properties of **1** and **2** is attributed to the constrained environment of the crystalline state.

In general, $\Delta E(S_1-T_1)$ increases with increasing frontier orbitals overlap. As demonstrated, HOMOs and LUMOs of **1** and **2** are similar in the gas phase, which explains very similar S_1−T_1 adiabatic energy separations. In the crystal lattice, complex **1** can more easily accommodate structural changes upon photoexcitation than complex **2**, which has less void space available. Therefore, complex **2** cannot undergo the observed relaxation from a bent to a more linear structure in the crystal packing to the same extent as in the gas phase. This implies a smaller HOMO−LUMO overlap and a reduced S_1−T_1 gap for **2** in comparison to **1**, being consistent with the observed experimental $\Delta E(S_1-T_1)$ value for **1**.

To provide computational support to this hypothesis, the molecular structures of **1** and **2** were recalculated with geometric constraints on the copper atoms. Specifically, the three interatomic Cu···Cu separations and the two $Cu_{(out)}$−$Cu_{(in)}$−$Cu_{(in)}'$ angles were constrained to the values of the crystal structure analyses. As a result, for **2**, $\Delta E(S_1-T_1)$ decreased from 1745 cm^{-1} (Figure S33) to 1447 cm^{-1}. By contrast, the S_1−T_1 energy separation of **1** only moderately increased from 1756 to 1758 cm^{-1}. This is conclusive because complex **1** is already almost linear both in solid state and in the gas phase, whereas complex **2** cannot adopt a similar, more linear geometry through molecular motion, which is limited by less available void space in the crystal lattice.

CONCLUSIONS

We have demonstrated that flexible ethylene-bridged bis(amidinates) cleanly convert mesitylcopper into homoleptic Cu^I bis(amidinates) that form linear tetranuclear clusters with a disconnected ($Cu^I_{(out)}$···$Cu^I_{(in)}$)($Cu^I_{(in)}'$···$Cu^I_{(out)}'$) chain or continuous Cu^I_4 chains that are helically bent. Upon crystallization from toluene/diethyl ether mixtures or pure

https://doi.org/10.1021/acs.inorgchem.4c01646
Inorg. Chem. 2024, 63, 12943−12957

diethyl ether, larger octa- and decanuclear cluster assemblies are formed. This interrelation is shown in Scheme 6. All clusters **I**, **II**, and **1**−**3** are potent blue or green/yellow light emitters in the solid state and exhibit red-shifted emissions with increasing aggregation size.

Scheme 6. Overview and Interrelation of Complexes I, II, and 1−3

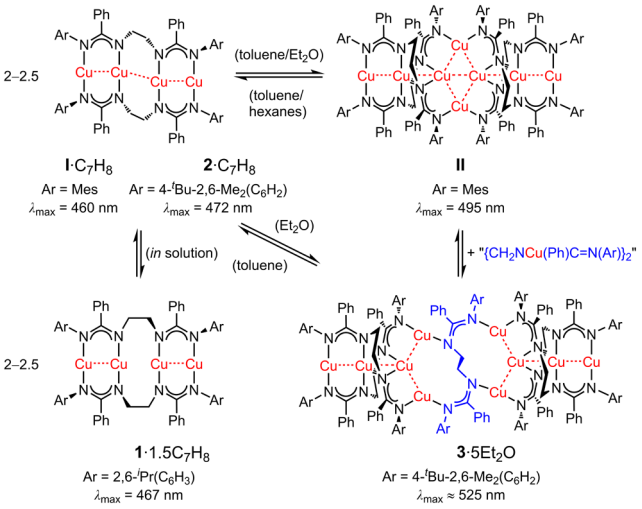

Based on DFT/TD-DFT calculations for the gas phase, it could be shown that the observed emission of **1** and **2** originates from MLCT transitions. This central $Cu^{I}_{(in)}\cdots Cu^{I}_{(in)}{}'$ contact, connecting the two discrete Cu^{I}_{2} diamidinate segments to a twisted molecular torsion spring, is, in the crystalline state, already present (complex **2**) or, based on the correlation of the TD-DFT calculations with the emission behavior, established upon photoexcitation (complex **1**).

The choice of terminal aromatic substituents in combination with solvent and solvent polarity allows for controlling defined molecular structures through crystallization and consequently adjustable emission properties. These factors not only influence the size of the clusters (and therefore the emission wavelengths) but also the available void space in the crystal lattice (and therefore phosphorescence or TADF behavior).

Future work will be devoted to two major directions: first, control of the aggregation size of the Cu^{I} bis(amidinate) clusters through solubility and solvent polarity. Second, control of the void space in the crystal lattices through ligand design and cocrystallization of suitable solvent molecules that reduce the available void space to promote TADF behavior by reduced molecular motion of the embedded emissive clusters.

EXPERIMENTAL SECTION AND COMPUTATIONAL DETAILS

General Procedures. All synthetic procedures were carried out by using Schlenk or glovebox techniques under an atmosphere of dry argon. Glassware and NMR tubes were heat-sealed with a heat gun under vacuum. *Caution! Extreme care should be taken both in the handling of the cryogen liquid nitrogen and its use in the Schlenk line trap to avoid the condensation of oxygen from air. Solvents*: prior to use, diethyl ether (EMD, ≥99.0%), hexanes (mixture of isomers, BDH, ≥98.5%), and toluene (BDH, ≥99.5%) were freshly distilled from sodium/benzophenone. Alternatively, the aforementioned solvents were purified using a PPT Solvent Purification System. Dichloromethane (VWR, ≥99.5%) was freshly distilled from CaH_2. *Deuterated solvents*: DMSO-d_6 (Cambridge Isotope Laboratories, Inc., D, 99.9 + 0.03% v/v tetramethylsilane, TMS) was used as purchased. C_6D_6 (Cambridge Isotope Laboratories, Inc., D, 99.5%) was distilled from sodium. *Reactants*: triethylamine (Alfa Aesar, 99%) was distilled from sodium. Ethylene diamine (Acros, 99+%) was dried over molecular sieves (3 Å). 2,6-Diisopropylaniline (Alfa Aesar, 90+%), 2,6-dimethyl-4-^{t}butylaniline (Matrix Scientific, 97%), benzoic acid (Alfa Aesar, ≥99.5%), *N*,*N*′-carbonyldiimidazole (Oakwood Chemicals), and PCl_5 (Alfa Aesar, 98%) were used as purchased. *N*,*N*′-1,2-ethanediylbis-(benzenecarboximidoyl chloride)[19,21] and mesitylcopper[35] were prepared according to literature procedures.[35a] Elemental analyses were performed by Atlantic Microlab, Inc. Melting points were determined with an SRS (Stanford Research Systems) Digi Melt instrument using open capillaries; values are uncorrected (the heating rate was 2 K/min). NMR measurements were recorded on a Bruker Avance III 400 spectrometer at ambient probe temperatures unless noted at 400.1 MHz (^{1}H) and 100.6 MHz (^{13}C), respectively. ^{13}C NMR resonances were obtained with proton broadband decoupling and referenced to the solvent signals of DMSO-d_6 at 39.5 and C_6D_6 at 128.0 ppm (^{1}H NMR: 2.50 (DMSO), and 7.15 (benzene), respectively). ^{13}C NMR assignments are based on COSY, NOESY, HSQC, and HMBC 2D experiments. Mass-spectrometric analyses were performed on a Bruker Ultraflex II TOF instrument (MALDI), on a Waters Q-Tof API US quadrupole time-of-flight MS system (low-resolution ESI), and on a Thermo Orbitrap Velos Pro MS system (high-resolution ESI). IR spectra were recorded on a PerkinElmer Spectrum One FT-IR spectrometer equipped with a Universal ATR Sampling Accessory.

General Procedure for the Preparation of L^1H_2 and L^2H_2. A solution of arylamine ($\mathbf{L}^1H_2$: 1.130 g, 6.37 mmol; $\mathbf{L}^2H_2$: 0.980 g, 5.53 mmol) in toluene (15 mL) was added dropwise to a solution of *N*,*N*′-1,2-ethanediylbis(benzenecarboximidoyl chloride) ($\mathbf{L}^1H_2$: 0.973 g, 3.19 mmol; $\mathbf{L}^2H_2$: 0.844 g, 2.77 mmol) in toluene (60 mL) at 0 °C with stirring. The reaction mixture was allowed to warm to room temperature for 30 min, then heated to reflux for 18 h, and subsequently cooled to room temperature. The resulting precipitate was isolated by filtration, washed with toluene (3 × 3 mL), and then suspended in a mixture of CH_2Cl_2 (60 mL) and 1 M aqueous solution of NaOH (60 mL). The organic phase was separated, first washed with 1 M aqueous solution of NaOH (2 × 40 mL), subsequently with deionized water (5 × 40 mL), then with brine (2 × 50 mL), and finally dried over anhydrous Na_2SO_4. After filtration, the solution was concentrated by rotary evaporation to about 5 mL. Storage at −35 °C overnight resulted in the formation of small colorless crystals. These were isolated by filtration and dried in oil pump vacuum for 18 h.

***L*^{1}*H*$_2$.** Yield: 1.138 g, (1.94 mmol, 61%). mp 145.8−146.9 °C; Anal. Calcd for $C_{40}H_{50}N_4$: C, 81.87; H, 8.59; N, 9.55. Found: C, 81.93; H, 8.39; N, 9.59. ^{1}H NMR (400.1 MHz, C_6D_6): δ 1.00 (s, ≈12H; CH_3, ^{i}Pr), 1.24 (s, ≈12H; CH_3′, ^{i}Pr), 3.27 (broad s with broad shoulder, ≈5H; CH_2 and CH, ^{i}Pr), 3.78 (broad s, ≈3H; CH_2), 5.13 (broad s, ≈2H; NH), 6.84, 7.06 (2 × s, 16H; CH, Dipp, Ph, overlaid by residual benzene signal), 7.81 (broad, CH, Dipp, Ph). ^{1}H NMR (400.1 MHz, DMSO-d_6): δ 0.86 (s, 12H; CH_3, ^{i}Pr), 1.06 (s, 12H; CH_3′, ^{i}Pr), 3.01 (s, 4H; CH, ^{i}Pr), 3.36−3.67 (broad m, 4H; CH_2), 6.79−6.87 (m, 6H; CH, Dipp, Ph), ≈7.04−7.22 (m, 12H; CH, Dipp, Ph, NH). ^{13}C{^{1}H} NMR (100.6 MHz, C_6D_6): δ 22.6 (CH_3, ^{i}Pr), 24.3 (CH_3′, ^{i}Pr), 28.7 (CH, ^{i}Pr), 42.9 (CH_2), 122.9, 123.3, 129.4 (CH, Dipp, Ph, two CH signals are likely overlaid by another signal or too broad to be detected), 135.2 (C, Dipp, Ph), 138.7 (C, *o*-Dipp), 145.7 (C, Dipp, Ph), 154.9 (C, CN_2). ^{13}C{^{1}H} NMR (100.6 MHz, DMSO-d_6): δ 22.1 (CH_3, ^{i}Pr), 23.7 (CH_3′, ^{i}Pr), 27.5 (CH, ^{i}Pr), 41.2 (broad, CH_2), 121.2, 122.2, 127.7, 128.8 (CH, Dipp, Ph, one CH signal is overlaid by another signal or too broad to be detected), 134.9 (C, Dipp, Ph), 137.6 (C, *o*-Dipp), 145.7 (C, Dipp, Ph) 154.0 (C, CN_2). MS (ESI(+)): *m*/*z* (relative intensity): 587 (7) $[M + H]^+$, 294 (100) $[M + 2H]^{2+}$. HRMS (ESI(+)): *m*/*z* calcd for $C_{40}H_{50}N_4$ $[M + H]^+$, 587.4108; found, 587.4107. IR (neat, cm^{-1}): 3368, 3306 (w, ν(N−H)), 3058 (w, ν(CH)), 2958, 2932, 2868 (m, ν(CH)), 1620 (vs), 1600, 1582, 1518 (s), 1494, 1452, 1432, 1392, 1374 (m), 1360 (w), 1312, 1300, 1282, 1260 (m), 1226, 1206, 1178 (w), 1140 (m), 1108,

https://doi.org/10.1021/acs.inorgchem.4c01646
Inorg. Chem. 2024, 63, 12943−12957

1098, 1074, 1052, 1024, 1012, 934, 920, 902, 834, 806 (w), 766 (vs), 738 (w), 700 (vs).

***L*²*H*₂.** Yield: 1.033 g, (1.76 mmol, 64%). mp 158.0−159.3 °C. Anal. Calcd for $C_{40}H_{50}N_4$: C, 81.87; H, 8.59; N, 9.55. Found: C, 81.21; H, 8.48; N, 9.31. ^{1}H NMR (400.1 MHz, C_6D_6): δ 1.26 (s, 18H; CH_3, ^{t}Bu), 2.16 (s, 12H; CH_3, 4-^{t}Bu-2,6-*Me*$_2$(C_6H_2)), 2.99 (broad s, ≈1H; CH_2), 3.76 (s, ≈3H; CH_2), 5.43 (broad s, ≈2H; NH), 6.77 (s, 5H; CH, Ph), 7.02 (s, 4H; CH, 4-^{t}Bu-2,6-Me$_2$(C_6H_2)), ≈7.02−7.15, 7.83 (broad, 10H; CH, Ph, overlaid by C_6H_6 signal). ^{1}H NMR (400.1 MHz, DMSO-*d*$_6$, 60 °C): δ 1.20 (s, 18H; CH_3, ^{t}Bu), 1.96 (s, 12H; CH_3, 4-^{t}Bu-2,6-*Me*$_2$(C_6H_2)), 3.63 (broad s, 4H; CH_2), 6.83 (s, 4H; CH, 4-^{t}Bu-2,6-Me$_2$(C_6H_2)), 7.02 (broad s, 2H; NH), 7.24−7.28 (m, 10H; CH, Ph). ^{13}C{^{1}H} NMR (100.6 MHz, C_6D_6): δ 19.4 (CH_3, 4-^{t}Bu-2,6-*Me*$_2$(C_6H_2)), 31.8 (CH_3, ^{t}Bu), 34.0 (C, ^{t}Bu), 43.1 (CH_2), 125.1 (CH, (4-^{t}Bu-2,6-Me$_2$(C_6H_2)), 127.6 (CH, Ph), ≈128 (CH, Ph, overlaid by C_6D_6/residual C_6H_6 signals), 129.3 (CH, Ph), 136.2 (C, *i*-Ph, *i*-,*o*-C, 4-^{t}Bu-2,6-Me$_2$(C_6H_2)), 143.9 (C, *p*-C, 4-^{t}Bu-2,6-Me$_2$(C_6H_2)), 146.1 (C, *i*-Ph, *i*-,*o*-C, 4-^{t}Bu-2,6-Me$_2$(C_6H_2)), 156.4 (C, CN_2) (one quaternary ^{13}C resonance is overlaid by another signal or too broad to be detected). ^{13}C{^{1}H} NMR (100.6 MHz, DMSO-*d*$_6$, 60 °C): δ 18.5 (CH_3, 4-^{t}Bu-2,6-*Me*$_2$(C_6H_2)), 31.2 (CH_3, ^{t}Bu), 33.3 (C, ^{t}Bu), 41.1 (CH_2), 123.9 (CH, (4-^{t}Bu-2,6-Me$_2$(C_6H_2)), 127.1, 127.6 (CH, *o*-,*m*-Ph), 129.0 (CH, *p*-Ph), 135.3, 142.9, 144.5 (C, *i*-Ph, 4-^{t}Bu-2,6-Me$_2$(C_6H_2)), 155.7 (C, CN_2). MS (ESI(+)): *m*/*z* (relative intensity): 587 (20) $[M + H]^+$, 531 (6) $[M - {}^t\text{Bu}]^{2+}$, 294 (100) $[M + 2H]^{2+}$. HRMS (ESI(+)): *m*/*z* calcd for $C_{40}H_{50}N_4$ $[M + H]^+$, 587.4108; found 587.4103. IR (neat, cm^{-1}): 3404 (m, ν(N−H)), 3058, 3051, 3033, 2991 (w, ν(CH)), 2949, 2934, 2920 (m, ν(CH)), 2901, 2869, 2863 (w, ν(CH)), 1635 (vs), 1598 (s), 1576, 1558, 1553 (w), 1505 (s), 1479 (vs), 1461 (m), 1441 (s), 1408, 1391, 1374 (w), 1359 (m), 1323 (w), 1292 (vs), 1231 (w), 1211 (m), 1176 (w), 1147 (m), 1115 (s), 1074, 1038, 1029 (w), 992 (m), 945, 937, 920, 894, 884 (w), 872 (s), 849, 801 (w), 777, 754 (s), 700 (vs).

General Procedure for the Preparation of 1−3 ([L¹Cu₂]*n*, [L²Cu₂]*n*). To a stirred solution of mesitylcopper (100 mg, 0.547 mmol) in toluene (10 mL) was added a solution of $L^{1,2}H_2$ (161 mg, 0.274 mmol) in toluene (10 mL) dropwise at −35 °C by means of a cannula. The reaction mixture was allowed to warm to room temperature and stirred for 1 d at this temperature. In the following, the reaction mixture was filtered through a pad of diatomaceous earth (1 cm × 1 cm). The resulting solution was evaporated to dryness by using oil pump vacuum. The resulting solid was subsequently washed with cold (−35 °C) diethyl ether (3 × 2 mL) and hexanes (3 × 2 mL) and then isolated by filtration. Drying in oil pump vacuum for about 18 h resulted in a colorless ($[L^1Cu_2]_n$) or a bright citreous powder ($[L^2Cu_2]_n$). Crystallization of $[L^1Cu_2]_n$ from toluene yielded **1**·1.5C_7H_8. Crystallization of $[L^2Cu_2]_n$ from toluene yielded **2**·C_7H_8 and from diethyl ether **3**·5Et_2O, respectively (see the crystallographic section for details).

***[L¹Cu₂]n*.** Yield: 134 mg, (0.188 mmol, 69%). mp 240−260 °C (decomposition into a brown oil). Anal. Calcd for $C_{80}H_{96}N_8Cu_4$: C, 67.48; H, 6.80; N, 7.87. Found: C, 67.15; H, 6.86; N, 6.87. ^{1}H NMR (400.1 MHz, C_6D_6): δ 1.25 (s, 24H; CH_3, ^{i}Pr), 1.26 (s, 24H; CH_3', ^{i}Pr), 3.44 (s, 8H; CH_2), 3.71 (dq, $^3J_{H,H}$ = 6.6 Hz, 8H; CH, ^{i}Pr), 6.68 (t, $^3J_{H,H}$ = 7.3 Hz, 4H; *p*-Ph), 6.85 (s with broad shoulder, 20H; *m*-Ph, *m*-, *p*-Dipp), 7.05 (broad s, 8H; *o*-Ph). ^{13}C{^{1}H} NMR (100.6 MHz, C_6D_6): δ 22.3 (CH_3, ^{i}Pr), 24.7 (CH_3', ^{i}Pr), 28.3 (CH, ^{i}Pr), 57.7 (C, CH_2), 123.0 (CH, *m*-Dipp), 124.9 (CH, *p*-Dipp), 127.8−128.5 (3 × CH, *o*-, *m*-, *p*-Ph, overlaid by C_6D_6/residual C_6H_6 signals), 136.7 (C, *i*-Ph), 142.9 (C, *o*-Dipp), 143.4 (C, *i*-Dipp), 176.7 (C, CN_2). MS (ESI(+)): *m*/*z* (relative intensity): 1297.7 (0.1) $[(L^1H_2)(L^1H)Cu_2]^+$, 1235.7 (5.3) $[(L^1H)_2Cu]^+$, 649.3 (6.8) $[(L^1H)Cu + H]^+$, 587.4 (79.8) $[L^1H_2 + H]^+$, 294.2 (100) $[L^1H_2 + 2H]^{2+}$. IR (neat, cm^{-1}): 3059, 3026 (w, ν(CH)), 2958 (m, ν(CH)), 2925, 2918, 2888, 2869, 2865, 2860, 2848 (w, ν(CH)), 1603, 1579 (w), 1487, 1430 (vs), 1380, 1359, 1342 (m), 1319, 1257 (s), 1234, 1210 (m), 1178, 1157 (w), 1140 (m), 1096 (vs), 1080, 1076, 1056, 1040 (s), 1026 (vs), 933, 919, 866 (m), 846 (w), 820 (s), 793 (vs), 786 (vs), 767 (s), 753, 745 (m), 726 (s), 700, 693 (vs), 661 (s).

***[L²Cu₂]n*.** Yield: 127 mg, (0.178 mmol, 68%). mp 240−260 °C (decomposition into a brown oil). Anal. Calcd for $C_{80}H_{96}N_8Cu_4$: C, 67.48; H, 6.80; N, 7.87. Found: C, 67.33; H, 6.72; N, 7.85. ^{1}H NMR (400.1 MHz, C_6D_6): δ 1.02 (s, 36H; CH_3, ^{t}Bu), 2.65 (s, 24H; CH_3, 4-^{t}Bu-2,6-*Me*$_2$(C_6H_2)), 3.21 (s, 8H; CH_2), 6.68 (t, $^3J_{H,H}$ = 7.4 Hz, 4H; *p*-Ph), 6.77−6.81 (m, 8H; *m*-Ph, overlaid by *m*-CH signal, 4-^{t}Bu-2,6-Me$_2$(C_6H_2)), 6.81 (s, 8H; *m*-CH, 4-^{t}Bu-2,6-Me$_2$(C_6H_2)), overlaid by *m*-CH signal, Ph), 7.10 (d, $^3J_{H,H}$ = 7.4 Hz, 8H; *o*-CH, Ph). ^{13}C{^{1}H} NMR (100.6 MHz, C_6D_6): δ 20.5 (CH_3, 4-^{t}Bu-2,6-*Me*$_2$(C_6H_2)), 31.3 (CH_3, ^{t}Bu), 33.8 (C, ^{t}Bu), 55.2 (CH_2), 125.0 (*m*-CH, 4-^{t}Bu-2,6-Me$_2$(C_6H_2)), 126.9 (CH, *o*-Ph), 127.6 (CH, *m*-Ph), 127.6−128.2 (CH, *p*-Ph, overlaid by C_6D_6/residual C_6H_6 signals), 132.2 (*o*-C, 4-^{t}Bu-2,6-Me$_2$(C_6H_2)), 137.2 (C, *i*-Ph), 144.2 (*i*-C, 4-^{t}Bu-2,6-Me$_2$(C_6H_2)), 145.7 (*p*-C, 4-^{t}Bu-2,6-Me$_2$(C_6H_2)), 176.4 (C, CN_2). MS (ESI(+)): *m*/*z* (relative intensity): 1359.6 (<0.1) $[(L^2H)_2Cu_3]^+$, 1297.7 (0.3) $[(L^2H_2)(L^2H)Cu_2]^+$, 1235.7 (3.6) $[(L^2H)_2Cu]^+$, 1173.8 (0.4) $[(L^2H_2)_2 + H]^+$, 649.3 (6.0) $[(L^2H)Cu + H]^+$, 587.4 (81.5) $[L^2H_2 + H]^+$, 531.3 (7.7) $[L^2H - {}^t\text{Bu} + H]^+$, 294.2 (100) $[L^2H_2 + 2H]^{2+}$. IR (neat, cm^{-1}): 3060, 3050, 3028 (w, ν(CH)), 2961, 2950 (m, ν(CH)), 2932, 2927, 2917, 2903, 2869, 2863, 2849, 2843 (w, ν(CH)), 1604, 1580, 1559 (w), 1514 (s), 1489, 1429 (vs), 1393 (m), 1370 (w), 1361, 1350 (m), 1342 (s), 1304 (m), 1286 (w), 1267, 1250 (m), 1218 (s), 1177 (w), 1153 (m), 1117 (w), 1092 (m), 1073, 1063 (w), 1038 (w), 1027 (m), 989, 953, 943, 921 (w), 873 (m), 862, 849 (w), 805 (m), 780 (w), 765 (s), 728 (m), 703 (vs), 681 (m), 665 (w).

Photoluminescence Measurements. PL measurements were performed on a Horiba Jobin Yvon Fluorolog-322 spectrometer. Solid samples (crystalline powders) were measured as dispersions in a thin layer of viscous perfluoropolyether oil between two quartz plates. The latter were mounted in one of two closed-cycle optical cryostats (operating temperature ranges: ≈20−300 and 3−300 K). All emission spectra were corrected for the wavelength-dependent response of the spectrometer and detector (in relative photon flux units). Emission decay traces were recorded by connecting a Fluorolog photomultiplier to a fast digital oscilloscope (via a 50, 500, or 2500 Ω load depending on the decay time scale) and using a nitrogen laser for pulsed excitation (337 nm, ∼2 ns, ∼5 μJ per pulse). PL quantum yields of **1**−**3** at ambient temperature were determined using an integrating sphere out of optical PTFE, which was installed into the sample chamber of the spectrometer. The accuracy of the quantum yield measurements is estimated as ±10%. PL of microcrystals of **1**−**3** under high hydrostatic pressure was recorded on the Fluorolog spectrometer at ambient temperature using a diamond anvil cell (DAC) with ≈0.8 mm anvils (Diacell Ltd.). Perfluoropolyether or mineral oil was applied as a pressure transmitting medium. Similar to PL measurements with the optical cryostat, the emission from DAC was collected at ≈30° relative to the excitation beam. Further experimental details can be found in ref 43.

X-ray Crystallography. Colorless plates of L^1H_2, tabular yellow plates of **2**·C_7H_8, and bright yellow blocks of **3**·5Et_2O suitable for XRD analysis were obtained from concentrated diethyl ether (L^1H_2, −35 °C, and **3**·5Et_2O, room temperature) and toluene (**2**·C_7H_8, −35 °C) solutions, respectively. Single crystals of L^2H_2 and **1**·1.5C_7H_8 were grown as colorless blocks from a slowly evaporating diethyl ether (L^2H_2) or toluene (**1**·1.5C_7H_8) solutions at room temperature. X-ray data for L^1H_2, L^2H_2, **1**·1.5C_7H_8, **2**·C_7H_8, and **3**·5Et_2O were collected on a Bruker Venture X-ray diffractometer (Cu Ka radiation, λ = 1.54178 Å or Mo Ka radiation, λ = 0.71073 Å) by using ω and φ scans at 100 K (L^1H_2, L^2H_2, **1**·1.5C_7H_8, and **3**·5Et_2O) or 140 K (**2**·C_7H_8, Table S1). The integrated intensities for each reflection were obtained by reduction of the data frames with the program APEX3.[44] Cell parameters were obtained and refined with 41,386 (11,722 unique, L^1H_2), 13,487 (3379 unique, L^2H_2), 9294 (9294 unique, **1**·1.5C_7H_8), and 42,319 (9791 unique, **2**·C_7H_8) and 764,415 (79,089 unique, **3**·5Et_2O) reflections, respectively. The integrated data for L^1H_2, L^2H_2, and **2**·C_7H_8 and **3**·5Et_2O were corrected for absorption by using SADABS.[45] For **1**·1.5C_7H_8, TWINABS[46] was used for integrated data correction as well as to generate hklf4 and hklf5 files, containing the reflection from the major component only (hklf4) and from both components (hklf5). While the hklf4 file was used for

https://doi.org/10.1021/acs.inorgchem.4c01646
Inorg. Chem. 2024, 63, 12943−12957

structure solution, hklf5 data served for the final least-squares refinement. The structures were solved by direct methods and refined (weighted least-squares refinement on F^2) by using SHELXL.[47] The hydrogen atoms were placed in idealized positions and refined by using a riding model. Non-hydrogen atoms were refined with anisotropic thermal parameters. For $\mathbf{L^2H_2}$, residual electron peaks indicated the presence of partially occupied and/or disordered solvent molecules which could not be successfully modeled. These were masked in the final refinement cycles for $\mathbf{L^2H_2}$ using the program Olex2.[48] Solvent molecules in $\mathbf{1}\cdot 1.5C_7H_8$, $\mathbf{2}\cdot C_7H_8$ and $\mathbf{3}\cdot 5Et_2O$ were successfully modeled using typical restraints (for example, SADI, SIMU). In $\mathbf{1}\cdot 1.5C_7H_8$, the toluene molecules are disordered by symmetry, with one in 0.5 occupancy disordered about an inversion center, and another in 0.25 occupancy disordered about a 2-fold rotation axis. In $\mathbf{3}\cdot 5Et_2O$, the site occupancies of disordered, overlapping solvent molecules, as well as those of some disordered ^{t}Bu groups were refined as free variables. For all structures, the absence of additional symmetry and void was confirmed using PLATON (ADDSYM).[49]

Computational Details. The crystallographically determined structures of **1**, **2**, and **3** were geometry-optimized using DFT with the PBE1PBE hybrid functional (also known as PBE0).[50] The choice of functional was motivated by previous computations on Cu(I) systems that indicate reasonable results with such hybrid functionals.[51] The Cu atoms were described using the 6-311+G* basis set, while C, N, and H atoms were described using 6-31G*. The same basis set was used in our previous report on complexes **I** and **II**.[19] No symmetry was enforced in the calculations. Frequency calculations were run to compute thermal corrections to the potential energy for the optimized structures.

Singlet and triplet excited state energies were computed for molecules **1** and **2** using the time-dependent DFT (TD-DFT) approach using the same functional and basis set. Excited state geometry optimizations were performed employing the appropriate excited-state gradients. Natural transition orbitals (NTOs) were computed to provide a more compact description of the excitation orbital character.[52]

■ ASSOCIATED CONTENT

Supporting Information

The Supporting Information is available free of charge at https://pubs.acs.org/doi/10.1021/acs.inorgchem.4c01646.

Crystallographic data of $\mathbf{L^1H_2}$, $\mathbf{L^1H_2}$, $\mathbf{1}\cdot 1.5C_7H_8$, $\mathbf{2}\cdot C_7H_8$, and $\mathbf{3}\cdot 5Et_2O$; computational details of **1**−**3**; ^{1}H and $^{13}C\{^1H\}$ NMR spectra of $\mathbf{L^1H_2}$, $\mathbf{L^1H_2}$, and **1**−**2**; and photoluminescence spectra of **1**−**3** (PDF)

Computed structure coordinates (ZIP)

Accession Codes

CCDC 2157306 ($\mathbf{L^1H_2}$), CCDC 2157307 ($\mathbf{L^2H_2}$), CCDC 2326575 ($\mathbf{1}\cdot 1.5C_7H_8$), CCDC 2119616 ($\mathbf{2}\cdot C_7H_8$), and CCDC 2119617 ($\mathbf{3}\cdot 5Et_2O$) contain the supplementary crystallographic data (CIF) for this paper. These data can be obtained free of charge via www.ccdc.cam.ac.uk/data_request/cif, or by emailing data_request@ccdc.cam.ac.uk, or by contacting The Cambridge Crystallographic Data Centre, 12 Union Road, Cambridge CB2 1EZ, UK; fax: +44 1223 336033.

■ AUTHOR INFORMATION

Corresponding Author

Michael Stollenz − *Department of Chemistry and Biochemistry, Kennesaw State University, Kennesaw, Georgia 30144, United States;* orcid.org/0000-0002-8635-164X; Email: Michael.Stollenz@kennesaw.edu

Authors

Janet Arras − *Department of Chemistry and Biochemistry, Kennesaw State University, Kennesaw, Georgia 30144, United States;* orcid.org/0000-0001-7175-676X

Alvaro Calderón-Díaz − *Department of Chemistry and Biochemistry, Kennesaw State University, Kennesaw, Georgia 30144, United States;* orcid.org/0000-0001-5815-4916

Sergei Lebedkin − *Institute of Nanotechnology, Karlsruhe Institute of Technology (KIT), 76344 Eggenstein-Leopoldshafen, Germany*

Samer Gozem − *Department of Chemistry, Georgia State University, Atlanta, Georgia 30303, United States;* orcid.org/0000-0002-6429-2853

Colin D. McMillen − *Department of Chemistry, Clemson University, Clemson, South Carolina 29634-0973, United States*

Nattamai Bhuvanesh − *Department of Chemistry, Texas A&M University, College Station, Texas 77842-3012, United States*

Complete contact information is available at: https://pubs.acs.org/10.1021/acs.inorgchem.4c01646

Notes

The authors declare no competing financial interest.

■ ACKNOWLEDGMENTS

We thank Dr. Sanjay Dutta for data collection on single crystals of $\mathbf{1}\cdot 1.5C_7H_8$ and help to solve the structure. We also thank Nimia Zoé Maya, Brandon Bell, and Connor O'Dea for experimental assistance. Dr. Michael D. Walla and Dr. William E. Cotham (Mass Spectrometry Center at the University of South Carolina) are acknowledged for recording mass spectra. The authors acknowledge support for providing computing resources by the Advanced Computer Services at Kennesaw State University and the Advanced Research Computing Technology and Innovation Core (ARCTIC) resources, which are supported by NSF Major Research Instrumentation (MRI) grant number CNS-1920024. The Department of Chemistry and Biochemistry and the College of Sciences and Mathematics (CSM) at Kennesaw State University are acknowledged for financial support. This material is based upon work supported by the National Science Foundation under Grants CHE-1800332 and CHE-2155153.

■ REFERENCES

(1) Bera, J. K.; Dunbar, K. R. Chain Compounds Based on Transition Metal Backbones: New Life for an Old Topic. *Angew. Chem. Int.Ed.* **2002**, *41*, 4453−4457.

(2) For representative reviews about EMACs, see: (a) Berry, J. F. *Multiple Bonds between Metal Atoms*; Cotton, F. A., Murillo, C. A., Walton, R. A., Eds.; Springer Science and Business Media, Inc.: New York, Boston, Dordrecht, London, Moscow, 2005; pp 669−706. (b) Georgiev, V. P.; Mohan, P. J.; DeBrincat, D.; McGrady, J. E. Low-symmetry distortions in Extended Metal Atom Chains (EMACs): Origins and consequences for electron transport. *Coord. Chem. Rev.* **2013**, *257*, 290−298. (c) Hua, S.-A.; Tsai, Y.-C.; Peng, S.-M. A Journey of Metal-metal Bonding beyond Cotton's Quadruple Bonds. *J. Chin. Chem. Soc.* **2014**, *61*, 9−26. (d) Hua, S.-A.; Cheng, M.-C.; Chen, C.-h.; Peng, S.-M. From Homonuclear Metal String Complexes to Heteronuclear Metal String Complexes. *Eur. J. Inorg. Chem.* **2015**, *2015*, 2510−2523.

(3) Thompson, L. K.; Dawe, L. N. Magnetic properties of transition metal (Mn(II), Mn(III), Ni(II), Cu(II)) and lanthanide (Gd(III), Dy(III), Tb(III), Eu(III), Ho(III), Yb(III)) clusters and [nxn] grids:

Isotropic exchange and SMM behaviour. *Coord. Chem. Rev.* **2015**, *289*−*290*, 13−31.
(4) Stollenz, M. Linear Copper Complex Arrays as Versatile Molecular Strings: Syntheses, Structures, Luminescence, and Magnetism. *Chem.—Eur. J.* **2019**, *25*, 4274−4298.
(5) (a) Schmidbaur, H. The fascinating implications of new results in gold chemistry. *Gold Bull.* **1990**, *23*, 11−21. (b) Schmidbaur, H. Ludwig Mond Lecture. High-carat gold compounds. *Chem. Soc. Rev.* **1995**, *24*, 391−400. (c) Schmidbaur, H.; Schier, A. Aurophilic interactions as a subject of current research: an up-date. *Chem. Soc. Rev.* **2012**, *41*, 370−412.
(6) (a) *Gold: Progress in Chemistry, Biochemistry and Technology*; Schmidbaur, H., Ed.; Wiley VCH: Weinheim, 1999. (b) *Gold Chemistry: Applications and Future Directions in the Life Sciences*; Mohr, F., Ed.; Wiley VCH: Weinheim, 2009.
(7) Pyykkö, P. Strong Closed-Shell Interactions in Inorganic Chemistry. *Chem. Rev.* **1997**, *97*, 597−636.
(8) Pyykkö, P. Theoretical Chemistry of Gold. *Angew. Chem. Int. Ed.* **2004**, *43*, 4412−4456.
(9) (a) Yam, V. W.-W.; Lo, K. K.-W.; Fung, W. K.-M.; Wang, C.-R. Design of luminescent polynuclear copper(I) and silver(I) complexes with chalcogenides and acetylides as the bridging ligands. *Coord. Chem. Rev.* **1998**, *171*, 17−41. (b) Yam, V. W.-W.; Lo, K. K.-W. Luminescent polynuclear d^{10} metal complexes. *Chem. Soc. Rev.* **1999**, *28*, 323−334. (c) Ford, P. C.; Cariati, E.; Bourassa, J. Photoluminescence Properties of Multinuclear Copper(I) Compounds. *Chem. Rev.* **1999**, *99*, 3625−3648. (d) Yam, V. W.-W.; Cheng, E. C.-C. Highlights on the recent advances in gold chemistry—a photophysical perspective. *Chem. Soc. Rev.* **2008**, *37*, 1806−1813. (e) Tiekink, E. R. T.; Kang, J.-G. Luminescence properties of phosphinegold(I) halides and thiolates. *Coord. Chem. Rev.* **2009**, *253*, 1627−1648. (f) He, X.; Yam, V. W.-W. Luminescent gold(I) complexes for chemosensing. *Coord. Chem. Rev.* **2011**, *255*, 2111−2123. (g) Lang, H.; Jakob, A.; Milde, B. Copper(I) Alkyne and Alkynide Complexes. *Organometallics* **2012**, *31*, 7661−7693. (h) Yam, V. W.-W.; Au, V. K.-M.; Leung, S. Y.-L. Light-Emitting Self-Assembled Materials Based on d^8 and d^{10} Transition Metal Complexes. *Chem. Rev.* **2015**, *115*, 7589−7728. (i) Gupta, A. K.; Orthaber, A. Alkynyl Coinage Metal Clusters and Complexes-Syntheses, Structures, and Strategies. *Chem.—Eur. J.* **2018**, *24*, 7536−7559.
(10) Fraga, S.; Saxena, K. M. S.; Karwowski, J. *Handbook of Atomic Data*; Elsevier Scientific Publishing Company: Amsterdam, Oxford, NY, 1976; pp 423−431.
(11) (a) Hsu, C.-W.; Lin, C.-C.; Chung, M.-W.; Chi, Y.; Lee, G.-H.; Chou, P.-T.; Chang, C.-H.; Chen, P.-Y. Systematic Investigation of the Metal-Structure-Photophysics Relationship of Emissive d^{10}-Complexes of Group 11 Elements: The Prospect of Application in Organic Light Emitting Devices. *J. Am. Chem. Soc.* **2011**, *133*, 12085−12099. (b) Yu-Tzu Li, E.; Jiang, T.-Y.; Chi, Y.; Chou, P.-T. Semi-quantitative assessment of the intersystem crossing rate: an extension of the El-Sayed rule to the emissive transition metal complexes. *Phys. Chem. Chem. Phys.* **2014**, *16*, 26184−26192.
(12) *For key discoveries, see:* (a) *first reported observation of TADF in Cu^I complexes:* Kirchhoff, J. R.; Gamache, R. E., Jr.; Blaskie, M. W.; Del Paggio, A. A.; Lengel, R. K.; McMillin, D. R. Temperature Dependence of Luminescence from $Cu(NN)_2^+$ Systems in Fluid Solution. Evidence for the Participation of Two Excited States. *Inorg. Chem.* **1983**, *22*, 2380−2384. (b) *First reported efficient TADF-based OLED:* Uoyama, H.; Goushi, K.; Shizu, K.; Nomura, H.; Adachi, C. Highly efficient organic light-emitting diodes from delayed fluorescence. *Nature* **2012**, *492*, 234−238. (c) Leitl, M. J.; Krylova, V. A.; Djurovich, P. I.; Thompson, M. E.; Yersin, H. Phosphorescence versus Thermally Activated Delayed Fluorescence. Controlling Singlet-Triplet Splitting in Brightly Emitting and Sublimable Cu(I) Compounds. *J. Am. Chem. Soc.* **2014**, *136*, 16032−16038. (d) Di, D.; Romanov, A. S.; Yang, L.; Richter, J. M.; Rivett, J. P. H.; Jones, S.; Thomas, T. H.; Abdi Jalebi, M.; Friend, R. H.; Linnolahti, M.; Bochmann, M.; Credgington, D. High-performance light-emitting diodes based on carbene-metal-amides. *Science* **2017**, *356*, 159−163. (e) Hamze, R.; Peltier, J. L.; Sylvinson, D.; Jung, M.; Cardenas, J.; Haiges, R.; Soleilhavoup, M.; Jazzar, R.; Djurovich, P. I.; Bertrand, G.; Thompson, M. E. Eliminating nonradiative decay in Cu(I) emitters: > 99% quantum efficiency and microsecond lifetime. *Science* **2019**, *363*, 601−606. (f) Schinabeck, A.; Chen, J.; Kang, L.; Teng, T.; Homeier, H. H. H.; Suleymanova, A. F.; Shafikov, M. Z.; Yu, R.; Lu, C.-Z.; Yersin, H. Symmetry-Based Design Strategy for Unprecedentedly Fast Decaying Thermally Activated Delayed Fluorescence (TADF). Application to Dinuclear Cu(I) Compounds. *Chem. Mater.* **2019**, *31*, 4392−4404. (g) Olaru, M.; Rychagova, E.; Ketkov, S.; Shynkarenko, Y.; Yakunin, S.; Kovalenko, M. V.; Yablonskiy, A.; Andreev, B.; Kleemiss, F.; Beckmann, J.; Vogt, M. A Small Cationic Organo-Copper Cluster as Thermally Robust Highly Photo- and Electroluminescent Material. *J. Am. Chem. Soc.* **2020**, *142*, 373−381. (h) Klein, M.; Rau, N.; Wende, M.; Sundermeyer, J.; Cheng, G.; Che, C.-M.; Schinabeck, A.; Yersin, H. Cu(I) and Ag(I) Complexes with a New Type of Rigid Tridentate N,P,P-Ligand for Thermally Activated Delayed Fluorescence and OLEDs with High External Quantum Efficiency. *Chem. Mater.* **2020**, *32*, 10365−10382.
(13) *For representative reviews see:* (a) Yersin, H.; Rausch, A. F.; Czerwieniec, R.; Hofbeck, T.; Fischer, T. The triplet state of organo-transition metal compounds. Triplet harvesting and singlet harvesting for efficient OLEDs. *Coord. Chem. Rev.* **2011**, *255*, 2622−2652. (b) Leitl, M. J.; Zink, D. M.; Schinabeck, A.; Baumann, T.; Volz, D.; Yersin, H. Copper(I) Complexes for Thermally Activated Delayed Fluorescence: From Photophysical to Device Properties. *Top. Curr. Chem. (Z)* **2016**, *374*, 25. (c) Yersin, H.; Czerwieniec, R.; Shafikov, M. Z.; Suleymanova, A. F. TADF Material Design: Photophysical Background and Case Studies Focusing on Cu^I and Ag^I Complexes. *ChemPhysChem* **2017**, *18*, 3508−3535. (d) Bizzarri, C.; Spuling, E.; Knoll, D. M.; Volz, D.; Bräse, S. Sustainable metal complexes for organic light-emitting diodes (OLEDs). *Coord. Chem. Rev.* **2018**, *373*, 49−82. (e) Liu, Y.; Yiu, S.-C.; Ho, C.-L.; Wong, W.-Y. Recent advances in copper complexes for electrical/light energy conversion. *Coord. Chem. Rev.* **2018**, *375*, 514−557. (f) Ravaro, L. P.; Zanoni, K. P. S.; de Camargo, A. S. S. Luminescent Copper(I) complexes as promising materials for the next generation of energy-saving OLED devices. *Energy Rep.* **2020**, *6*, 37−45. (g) Beaudelot, J.; Oger, S.; Peruško, S.; Phan, T.-A.; Teunens, T.; Moucheron, C.; Evano, G. Photoactive Copper Complexes: Properties and Applications. *Chem. Rev.* **2022**, *122*, 16365−16609.
(14) (a) Carvajal, M. A.; Alvarez, S.; Novoa, J. J. The Nature of Intermolecular $Cu^I\cdots Cu^I$ Interactions: A Combined Theoretical and Structural Database Analysis. *Chem.—Eur. J.* **2004**, *10*, 2117−2132. (b) Dinda, S.; Samuelson, A. G. The Nature of Bond Critical Points in Dinuclear Copper(I) Complexes. *Chem.—Eur. J.* **2012**, *18*, 3032−3042.
(15) (a) Oakley, S. H.; Coles, M. P.; Hitchcock, P. B. Structural Consequences of the Prohibition of Hydrogen Bonding in Copper-Guanidine Systems. *Inorg. Chem.* **2004**, *43*, 5168−5172. (b) Zheng, S.-L.; Messerschmidt, M.; Coppens, P. An Unstable Ligand-Unsupported Cu^I Dimer Stabilized in a Supramolecular Framework. *Angew. Chem. Int. Ed.* **2005**, *44*, 4714−4617. (c) Chiarella, G. M.; Melgarejo, D. Y.; Rozanski, A.; Hempte, P.; Pérez, L. M.; Reber, C.; Fackler, J. P., Jr. A short, unsupported Cu(I)···Cu(I) interaction, 2.65 Å, in a dinuclear guanidine chloride complex. *Chem. Commun.* **2010**, *46*, 136−138.
(16) Bondi, A. van der Waals Volumes and Radii. *J. Phys. Chem.* **1964**, *68*, 441−451.
(17) Edelmann, F. T. Advances in the Coordination Chemistry of Amidinate and Guanidinate Ligands. *Adv. Organomet. Chem.* **2008**, *57*, 183−352.
(18) (a) Cotton, F. A.; Feng, X.; Matusz, M.; Poli, R. Experimental and theoretical studies of the copper(I) and silver(I) dinuclear N,N′-di-p-tolylformamidinato complexes. *J. Am. Chem. Soc.* **1988**, *110*, 7077−7083. (b) Maier, S.; Hiller, W.; Strähle, J.; Ergezinger, C.; Dehnicke, K. $Cu_2[Ph\text{-}C(NSiMe_3)_2]_2$, an Amidinato Complex with a Short Cu - Cu Distance. *Z. Naturforsch. B* **1988**, *43*, 1628−1632.

https://doi.org/10.1021/acs.inorgchem.4c01646
Inorg. Chem. 2024, 63, 12943−12957

(c) Jiang, X.; Bollinger, J. C.; Baik, M.-H.; Lee, D. Copper clusters built on bulky amidinate ligands: spin delocalization *via* superexchange rather than direct metal-metal bonding. *Chem. Commun.* **2005**, 1043−1045. (d) Jiang, X.; Bollinger, J. C.; Lee, D. How Bulky Is a Bulky Ligand: Energetic Consequences of Steric Constraint in Ligand-Directed Cluster Assembly and Disassembly. *J. Am. Chem. Soc.* **2005**, *127*, 15678−15679.

(19) Stollenz, M.; Raymond, J. E.; Pérez, L. M.; Wiederkehr, J.; Bhuvanesh, N. Highly Luminescent Linear Complex Arrays of up to Eight Cuprous Centers. *Chem.—Eur. J.* **2016**, *22*, 2396−2405.

(20) Harisomayajula, N. V. S.; Wu, B.-H.; Lu, D.-Y.; Kuo, T.-S.; Chen, I.-C.; Tsai, Y.-C. Ligand-Unsupported Cuprophilicity in the Preparation of Dodecacopper(I) Complexes and Raman Studies. *Angew. Chem. Int. Ed.* **2018**, *57*, 9925−9929.

(21) Calderón-Díaz, A.; Arras, J.; Miller, E. T.; Bhuvanesh, N.; McMillen, C. D.; Stollenz, M. Ethylene-Bridged Tetradentate Bis(amidines): Supramolecular Assemblies through Hydrogen Bonding and Photoluminescence upon Deprotonation. *Eur. J. Org Chem.* **2020**, *2020*, 3243−3250.

(22) O'Dea, C.; Ugarte Trejo, O.; Arras, J.; Ehnbom, A.; Bhuvanesh, N.; Stollenz, M. Ethylene-bridged Hexadentate Bis(amidines) and Bis(amidinates) with Variable Binding Sites. *J. Org. Chem.* **2019**, *84*, 14217−14226.

(23) Group 1: (a) Whitener, G. D.; Hagadorn, J. R.; Arnold, J. Synthesis and characterization of a new class of chelating bis(amidinate) ligands. *J. Chem. Soc., Dalton Trans.* **1999**, 1249−1256. (b) Baker, R. J.; Jones, C. J. Synthesis and characterisation of sterically bulky lithium amidinate and bis-amidinate complexes. *J. Organomet. Chem.* **2006**, *691*, 65−71. (c) Hill, M. S.; Hitchcock, P. B.; Mansell, S. M. Racemic N-aryl bis(amidines) and bis(amidinates): on the trail of enantioselective organolanthanide catalysts. *Dalton Trans.* **2006**, 1544−1553. (d) Bai, S.-D.; Guo, J.-P.; Liu, D.-S. A convenient route to silyl linked bis(amidinate) ligands and synthesis of group(I) metal derivatives. *Dalton Trans.* **2006**, 2244−2250. (e) Skvortsov, G. G.; Fukin, G. K.; Ketkov, S. Yu.; Cherkasov, A. V.; Lyssenko, K. A.; Trifonov, A. A. Benzonitrile Insertion into Silylarylamides − *ansa*-Bis(benzamidinate) Ligand Systems with Rigid *o*- and *m*-Phenylene Linkers in the Synthesis of Lithium and Rare Earth Complexes. *Eur. J. Inorg. Chem.* **2013**, *2013*, 4173−4183. (f) Bai, S.-D.; Liu, R.-Q.; Guan, F.; Wang, T.; Tong, H.-B.; Guo, J.-P.; Liu, D.-S. Alkyl-ended *ansa*-bis(amidinate) ligands from aliphatic primary amines and multinuclear lithium derivatives. *Mendeleev Commun.* **2013**, *23*, 265−267. (g) Novotný, M.; Švec, P.; Růžičková, Z.; Růžička, A. Direct access to non-symmetric lithium nitriloamidinate and disymmetric dilithium bisamidinate complexes from 1,3- or 1,4-dicyanobenzene and lithium amides. *J. Organomet. Chem.* **2017**, *849−850*, 88−97. (h) Tolpygin, A. O.; Cherkasov, A. V.; Fukin, G. K.; Trifonov, A. A. Synthesis of New Bulky Bis(amidine) with the Conformationally Rigid *meta*-Phenylene Bridge and Its Dilithium Derivative $[1,3\text{-}C_6H_4\{NC(Ph)N(2,6\text{-}iso\text{-}Pr_2C_6H_3)\}_2]Li_2(TMEDA)_2$. *Russ. J. Coord. Chem.* **2019**, *45*, 288−294.

(24) Group 2: Rösch, A.; Schreiner, S. H. F.; Schüler, P.; Görls, H.; Kretschmer, R. Magnesium bis(amidinate) and bis(guanidinate) complexes: impact of the ligand backbone and bridging groups on the coordination behaviour. *Dalton Trans.* **2020**, *49*, 13072−13082.

(25) Group 3: see also ref 23e. (a) Bambirra, S.; Meetsma, A.; Hessen, B.; Teuben, J. H. Yttrium Alkyl Complex with a Linked Bis(amidinate) Ancillary Ligand. *Organometallics* **2001**, *20*, 782−785. (b) Wang, J.; Cai, T.; Yao, Y.; Zhang, Y.; Shen, Q. Ytterbium amides of linked bis(amidinate): synthesis, molecular structures, and reactivity for the polymerization of L-lactide. *Dalton Trans.* **2007**, 5275−5281. (c) Wang, J.; Sun, H.; Yao, Y.; Zhang, Y.; Shen, Q. Bridged bis(amidinate) lanthanide complexes: Synthesis, molecular structure and reactivity. *Polyhedron* **2008**, *27*, 1977−1982. (d) Wang, J.; Li, J.; Xu, F.; Shen, Q. Anionic Bridged Bis(amidinate) Lithium Lanthanide Complexes: Efficient Bimetallic Catalysts for Mild Amidation of Aldehydes with Amines. *Adv. Synth. Catal.* **2009**, *351*, 1363−1370. (e) Wang, J.; Yao, Y.; Zhang, Y.; Shen, Q. Bridged Bis(amidinate) Ytterbium Alkoxide and Phenoxide: Syntheses, Structures, and Their High Activity for Controlled Polymerization of L-Lactide and ε-Caprolactone. *Inorg. Chem.* **2009**, *48*, 744−751. (f) Skvortsov, G. G.; Tolpyguin, A. O.; Fukin, G. K.; Cherkasov, A. V.; Trifonov, A. A. Dinuclear Chlorido-, Alkyl(chlorido)-, and Hydridoyttrium Complexes Supported by μ-Bridging-Silyl-Linked Bis(amidinate) Ligands. *Eur. J. Inorg. Chem.* **2010**, *2010*, 1655−1662. (g) Yakovenko, M. V.; Cherkasov, A. V.; Fukin, G. K.; Cui, D.; Trifonov, A. A. Lanthanide Complexes Coordinated by a Dianionic Bis(amidinate) Ligand with a Rigid Naphthalene Linker. *Eur. J. Inorg. Chem.* **2010**, *2010*, 3290−3298. (h) Pan, C.-L.; Chen, W.; Su, S.; Pan, Y.-S.; Wang, J. Cubic and doubly-fused cubic samarium clusters from Sm(II)-mediated reduction of organic azides and azobenzenes. *Dalton Trans.* **2011**, *40*, 7941−7945. (i) Yan, L.; Liu, H.; Wang, J.; Zhang, Y.; Shen, Q. Divalent Lanthanide Complexes Supported by the Bridged Bis(amidinates) L $[L = Me_3SiN(Ph)CN(CH_2)_3NC(Ph)NSiMe_3]$: Synthesis, Molecular Structures and One-Electron-Transfer Reactions. *Inorg. Chem.* **2012**, *51*, 4151−4160. (j) Li, W.; Xue, M.; Xu, F.; Tu, J.; Zhang, Y.; Shen, Q. Synthesis, characterization of bridged bis(amidinate) lanthanide amides and their application as catalysts for addition of amines to nitriles for monosubstituted *N*-arylamidines. *Dalton Trans.* **2012**, *41*, 8252−8260. (k) Tolpygin, A. O.; Shavyrin, A. S.; Cherkasov, A. V.; Fukin, G. K.; Trifonov, A. A. Chloro and Alkyl Rare-Earth Complexes Supported by *ansa*-Bis(amidinate) Ligands with a Rigid *o*-Phenylene Linker. Ligand Steric Bulk: A Means of Stabilization or Destabilization? *Organometallics* **2012**, *31*, 5405−5413. (l) Li, W.; Xue, M.; Tu, J.; Zhang, Y.; Shen, Q. Syntheses and structures of lanthanide borohydrides supported by a bridged bis(amidinate) ligand and their high activity for controlled polymerization of ε-caprolactone, L-lactide and *rac*-lactide. *Dalton Trans.* **2012**, *41*, 7258−7265. (m) Tu, J.; Li, W.; Xue, M.; Zhang, Y.; Shen, Q. Bridged bis(amidinate) lanthanide aryloxides: syntheses, structures, and catalytic activity for addition of amines to carbodiimides. *Dalton Trans.* **2013**, *42*, 5890−5901. (n) Li, M.; Hong, J.; Chen, Z.; Zhou, X.; Zhang, L. Synthesis, structure and reactivity of dinuclear rare earth metal bis(*o*-aminobenzyl) complexes bearing a 1,4-phenylenediamidinate co-ligand. *Dalton Trans.* **2013**, *42*, 8288−8297. (o) Tolpygin, A. O.; Skvortsov, G. G.; Cherkasov, A. V.; Fukin, G. K.; Glukhova, T. A.; Trifonov, A. A. Lanthanide Borohydrido Complexes Supported by *ansa*-Bis(amidinato) Ligands with a Rigid *o*-Phenylene Linker: Effect of Ligand Tailoring on Catalytic Lactide Polymerization. *Eur. J. Inorg. Chem.* **2013**, *2013*, 6009−6018. (p) Tolpygin, A. O.; Cherkasov, A. V.; Fukin, G. K.; Trifonov, A. A. Reversible Switching of Coordination Mode of ansa bis(Amidinate) Ligand in Ytterbium Complexes Driven by Oxidation State of the Metal Atom. *Inorg. Chem.* **2014**, *53*, 1537−1543. (q) Karmel, I. S. R.; Elkin, T.; Fridman, N.; Eisen, M. S. Dimethylsilyl bis(amidinate)actinide complexes: synthesis and reactivity towards oxygen containing substrates. *Dalton Trans.* **2014**, *43*, 11376−11387. (r) Yakovenko, M. V.; Udilova, N. Yu.; Glukhova, T. A.; Cherkasov, A. V.; Fukin, G. K.; Trifonov, A. A. Amido rare-earth complexes supported by an *ansa* bis(amidinate) ligand with a rigid 1,8-naphthalene linker: synthesis, structures and catalytic activity in *rac*-lactide polymerization and hydrophosphonylation of carbonyl compounds. *New J. Chem.* **2015**, *39*, 1083−1093. (s) Kazeminejad, N.; Munzel, D.; Gamer, M. T.; Roesky, P. W. Bis(amidinate) ligands in early lanthanide chemistry - synthesis, structures, and hydroamination catalysis. *Chem. Commun.* **2017**, *53*, 1060−1063. (t) Skvortsov, G. G.; Tolpygin, A. O.; Fukin, G. K.; Long, J.; Larionova, J.; Cherkasov, A. V.; Trifonov, A. A. Rare-Earth Complexes Coordinated by *ansa*-Bis(amidinate) Ligands with *m*-Phenylene, 2,6-Pyridinediyl, and $SiMe_2$ Linkers. *Eur. J. Inorg. Chem.* **2017**, *2017*, 4275−4284. (u) Yu, X.; Li, M.; Hong, J.; Zhou, X.; Zhang, L. Living 3,4-(Co)Polymerization of Isoprene/Myrcene and One-Pot Synthesis of a Polyisoprene Blend Catalyzed by Binuclear Rare-Earth Metal Amidinate Complexes. *Chem.—Eur. J.* **2019**, *25*, 2569−2576. (v) Kazeminejad, N.; Münzfeld, L.; Gamer, M. T.; Roesky, P. W. Mono- and bimetallic amidinate samarium complexes - synthesis, structure, and hydroamination catalysis. *Dalton Trans.* **2019**, *48*, 8153−8160. (w) Tolpygin, A. O.; Shavyrin, A. S.; Cherkasov, A. V.; Fukin, G. K.; del Rosal, I.; Maron, L.; Trifonov, A. A. Alternative (κ^1-

https://doi.org/10.1021/acs.inorgchem.4c01646
Inorg. Chem. 2024, 63, 12943−12957

N:η^6-arene *vs.* κ^2-N,N) coordination of a sterically demanding amidinate ligand: are size and electronic structure of the Ln ion decisive factors? *Dalton Trans.* **2019**, *48*, 8317−8326. (x) Wang, F.; Zhao, X.; Meng, X.; Wang, S. Rare-earth complexes supported by an ansa-bis(amidinate) ligand with a rigid *o*-phenylene linker: synthesis, structure, and catalytic activity for polymerization of cyclic esters. *Dalton Trans.* **2019**, *48*, 12193−12198.

(26) Group 4: (a) Hagadorn, J. R.; Arnold, J. Tethered Bis-Amidinates as Supporting Ligands: A Concerted Elimination/σ-π Rearrangement Reaction Forming an Unusual Titanium Arene Complex. *Angew. Chem. Int. Ed.* **1998**, *37*, 1729−1731. (b) Babcock, J. R.; Incarvito, C.; Rheingold, A. L.; Fettinger, J. C.; Sita, L. R. Double Heterocumulene Metathesis of Cyclic Bis-(trimethylsilylamido)stannylenes and Tethered Bimetallic Bisamidinates from the Resulting α,ω-Biscarbodiimides. *Organometallics* **1999**, *18*, 5729−5732. (c) Hagadorn, J. R. New binucleating ligands to support dizirconium organometallics. *Chem. Commun.* **2001**, 2144−2145. (d) Hagadorn, J. R.; McNevin, M. J.; Wiedenfeld, G.; Shoemaker, R. Dizirconium Complexes Supported by Preorganized Binucleating Bis(amidinates). *Organometallics* **2003**, *22*, 4818−4824. (e) Grundy, J.; Coles, M. P.; Hitchcock, P. B. Ambiphilic ligands from the 1,4-benzenebis(amidine) framework. *New J. Chem.* **2004**, *28*, 1195−1197. (f) McNevin, M. J.; Hagadorn, J. R. Dititanium Complexes of Preorganized Binucleating Bis(amidinates). *Inorg. Chem.* **2004**, *43*, 8547−8554. (g) Li, J.; Huang, S.; Weng, L.-H.; Liu, D. Synthesis and structural studies of some titanium and zirconium complexes with chiral bis(amide), amidinate or bis-(amidinate) ligands. *J. Organomet. Chem.* **2006**, *691*, 3003−3010. (h) Zhang, W.; Sita, L. R. Investigation of Dynamic Intra- and Intermolecular Processes within a Tether-Length Dependent Series of Group 4 Bimetallic Initiators for Stereomodulated Degenerative Transfer Living Ziegler−Natta Propene Polymerization. *Adv. Synth. Catal.* **2008**, *350*, 439−447. (i) Bai, S.-D.; Guo, J.-P.; Liu, D.-S.; Wong, W.-Y. Bulky-Hindrance-Controlled Ligand Transformation from Linked Bis(amidinate) to Linked Imido-Amidinate Promoted by a Mono(cyclopentadienyl)titanium Group. *Eur. J. Inorg. Chem.* **2006**, *2006*, 4903−4907. (j) Bai, S.-D.; Tong, H.-B.; Guo, J.-P.; Zhou, M.-S.; Liu, D.-S. Coordination chemistry of group 4 metal compounds with mixed-ligand, silyl-linked bis(amidinate) ligand and cyclopentadienyl. *Inorg. Chim. Acta* **2009**, *362*, 1143−1148. (k) Pan, C.-L.; Chen, W.; Song, S.; Zhang, H.; Li, X. Stabilization of Imidosamarium(III) Cubane by Amidinates. *Inorg. Chem.* **2009**, *48*, 6344−6346. (l) Bai, S.-D.; Tong, H.-B.; Guo, J.-P.; Zhou, M.-S.; Liu, D.-S.; Yuan, S.-F. Diverse coordination behaviors of the silyl-linked bis(amidinate) ligand $[SiMe_2\{NC(Ph)N(Ph)\}_2]^{2-}$ to zirconium center. *Polyhedron* **2010**, *29*, 262−269. (m) Tong, H.-B.; Li, M.; Bai, S.-D.; Yuan, S.-F.; Chao, J.-B.; Huang, S.; Liu, D.-S. A bulky silyl shift-directed synthesis of a silyl-linked amidinate-amidine and its Zr(IV) complex. *Dalton Trans.* **2011**, *40*, 4236−4241. (n) Bai, S.-D.; Guan, F.; Hu, M.; Yuan, S.-F.; Guo, J.-P.; Liu, D.-S. Mononuclear titanium compounds based on the silyl-linked bis(amidinate) ligand: synthesis, characterization and ethylene polymerization. *Dalton Trans.* **2011**, *40*, 7686−7688. (o) Bai, S.-D.; Liu, R.-Q.; Wang, T.; Guan, F.; Wu, Y. B.; Chao, J.-B.; Tong, H.-B.; Liu, D.-S. An alkyl-ended *ansa*-bis(amidine) and solvent-influenced complexation modes of its group IV metal derivatives. *Polyhedron* **2013**, *65*, 161−169. (p) Wang, T.; Zhao, J.-P.; Bai, S.-D. Tetrachlorido[N^2,$N^{2'}$-(dimethylsilanediyl)bis(*N*-*tert*-butyl-3-methylbenzimidamidato)-κ^2N^2,$N^{2'}$]hafnium(IV). *Acta Crystallogr.* **2013**, *E69*, m654.

(27) Group 13: (a) Jenkins, H. A.; Abeysekera, D.; Dickie, D. A.; Clyburne, J. A. C. Double lithiation of 2,4,6-triphenylbromobenzene: synthesis of bis-amidines and an aluminium bis-amidinate complex. *J. Chem. Soc., Dalton Trans.* **2002**, 3919−3922. (b) Grundy, J.; Coles, M. P.; Hitchcock, P. B. A new class of linked-bis(*N*,*N*′-dialkylamidinate) ligand: applications in the synthesis of bimetallic aluminium complexes. *J. Organomet. Chem.* **2002**, *662*, 178−187. (c) Clare, B.; Sarker, N.; Shoemaker, R.; Hagadorn, J. R. Synthesis and Characterization of Binucleating Bis(amidinate) Ligands and Their Dialuminum Complexes. *Inorg. Chem.* **2004**, *43*, 1159−1166. (d) Lei, Y.; Chen, F.; Luo, Y.; Xu, P.; Wang, Y.; Zhang, Y. Bimetallic amidinate aluminum methyl complexes: Synthesis, crystal structure and activity for ϵ-caprolactone polymerization. *Inorg. Chim. Acta* **2011**, *368*, 179−186. (e) Bayram, M.; Bläser, D.; Wölper, C.; Schulz, S. Syntheses and Structures of Bis-Amidinate-Alane Complexes. *Organometallics* **2014**, *33*, 2080−2087. (f) Rösch, A.; Seifert, F.; Vass, V.; Görls, H.; Kretschmer, R. Synthesis, structure, and catalytic activity of dinuclear aluminium bis(amidinate) and bis(guanidinate) complexes. *New J. Chem.* **2021**, *45*, 972−981.

(28) Group 14: Appel, S.; Weller, F.; Dehnicke, K. On the Reaction of Tin Tetrachloride with Hexakis(trimethylsilyl)-1,4-benzdiamidine. Crystal Structures of $C_6H_4[C(NSiMe_3)_2SnCl_3{\cdot}CH_3CN]_2$ and $[Na\text{benzo-15-crown-5}]_2SnCl_6$. *Z. Anorg. Allg. Chem.* **1990**, *583*, 7−16.

(29) Group 8: Kawaguchi, H.; Matsuo, T. Binuclear iron(II) complex from a linked-bis(amidinate) ligand: synthesis and its reaction with carbon monoxide. *Chem. Commun.* **2002**, 958−959.

(30) Group 9: (a) Moos, E. M. B.; González-Gallardo, S.; Radius, M.; Breher, F. Rhodium(I) Complexes of *N*-Aryl-Substituted Mono- and Bis(amidinates) Derived from Their Alkali Metal Salts. *Eur. J. Inorg. Chem.* **2018**, *2018*, 3022−3035. (b) Kaufmann, S.; Radius, M.; Moos, E.; Breher, F.; Roesky, P. W. Rhodium(I) and Iridium(I) Complexes of Ferrocenyl-Functionalized Amidinates and Bis-(amidinates): κ^2N-Coordination Versus Ferrocenyl Ortho-Metalation. *Organometallics* **2019**, *38*, 1721−1732.

(31) Group 10: (a) Ohashi, M.; Yagyu, A.; Yamagata, T.; Mashima, K. Tetraplatinum precursors for supramolecular assemblies: syntheses, crystal structures, and stereoselective self-assemblies of $[Pt_4(\mu\text{-}OCOCH_3)_6(\kappa^4\text{-}N_4\text{-}DArBp)]$ (DArBp = 1,3-bis(arylbenzamidinate)-propane). *Chem. Commun.* **2007**, 3103−3105. (b) Tanaka, S.; Yagyu, A.; Kikugawa, M.; Ohashi, M.; Yamagata, T.; Mashima, K. Rational Synthesis of Supramolecular Assemblies Based on Tetraplatinum Units: Synthesis, Characterization, and Selective Substitution Reactions of Four Different Pt_4 Clusters. *Chem.—Eur. J.* **2011**, *17*, 3693−3709. (c) Tanaka, S.; Mashima, K. Interaction of Ferrocene Moieties Across a Square Pt_4 Unit: Synthesis, Characterization, and Electrochemical Properties of Carboxylate-Bridged Bimetallic Pt_4Fe_n (n = 2, 3, and 4) Complexes. *Inorg. Chem.* **2011**, *50*, 11384−11393. (d) Tanaka, S.; Mashima, K. Unique stepwise substitution reaction of a mono(guanidinate)tetraplatinum complex with amidines, giving mono(amidinate)tetraplatinum complexes through mixed-ligand intermediate complexes. *Dalton Trans.* **2013**, *42*, 2831−2840.

(32) Group 11: (a) Liu, J.-F.; Min, X.; Lv, J.-Y.; Pan, F.-X.; Pan, Q.-J.; Sun, Z.-M. Ligand-Controlled Syntheses of Copper(I) Complexes with Metal−Metal Interactions: Crystal Structure and Relativistic Density Functional Theory Investigation. *Inorg. Chem.* **2014**, *53*, 11068−11074. (b) Arras, J.; Ugarte Trejo, O.; Bhuvanesh, N.; Stollenz, M. Non-conventional hydrogen bonding and dispersion forces that support embedding mesitylgold into a tailored bis-(amidine) framework. *Chem. Commun.* **2022**, *58*, 1418−1421. (c) Arras, J.; Ugarte Trejo, O.; Bhuvanesh, N.; McMillen, C. D.; Stollenz, M. Hydrogen bonds and dispersion forces serving as molecular locks for tailored Group 11 bis(amidine) complexes. *Inorg. Chem. Front.* **2022**, *9*, 3267−3281.

(33) Nitsch, J.; Lacemon, F.; Lorbach, A.; Eichhorn, A.; Cisnetti, F.; Steffen, A. Cuprophilic interactions in highly luminescent dicopper-(I)-NHC-picolyl complexes - fast phosphorescence or TADF? *Chem. Commun.* **2016**, *52*, 2932−2935.

(34) Siddique, Z. A.; Yamamoto, Y.; Ohno, T.; Nozaki, K. Structure-Dependent Photophysical Properties of Singlet and Triplet Metal-to-Ligand Charge Transfer States in Copper(I) Bis(diimine) Compounds. *Inorg. Chem.* **2003**, *42*, 6366−6378.

(35) (a) Meyer, E. M.; Gambarotta, S.; Floriani, C.; Chiesi-Villa, A.; Guastini, C. Polynuclear Aryl Derivatives of Group 11 Metals: Synthesis, Solid State-Solution Structural Relationship, and Reactivity with Phosphines. *Organometallics* **1989**, *8*, 1067−1079. (b) Eriksson, H.; Håkansson, M. Mesitylcopper: Tetrameric and Pentameric. *Organometallics* **1997**, *16*, 4243−4244. (c) Stollenz, M.; Meyer, F. Mesitylcopper - A Powerful Tool in Synthetic Chemistry. *Organometallics* **2012**, *31*, 7708−7727.

https://doi.org/10.1021/acs.inorgchem.4c01646
Inorg. Chem. 2024, 63, 12943−12957

(36) Six pairs of identical *E*/*Z*, *syn*/*anti* stereoisomers and four unique stereoisomers are possible for $\mathbf{L}^1H_2$ and $\mathbf{L}^2H_2$ if the NH protons reside on the more basic ethylene-diamino bridge and tautomerization is not taken into account.
(37) For a classification, see: Jeffrey, G. A. *An Introduction to Hydrogen Bonding*; Oxford University Press: New York, 1997.
(38) Allen, F. H.; Kennard, O.; Watson, D. G.; Brammer, L.; Orpen, A. G.; Taylor, R. Tables of bond lengths determined by *X*-ray and neutron diffraction. Part 1. Bond lengths in organic compounds. *J. Chem. Soc., Perkin Trans. 2* **1987**, S1−S19.
(39) These Torsion Angles Were Calculated with the Program DIAMOND: DIAMOND—Crystal and Molecular Structure Visualization (version 3.2i), CRYSTAL IMPACT, Dr. H. Putz Dr. K. Brandenburg GbR, Kreuzherrenstr. 102, 53227 Bonn (Germany).
(40) The τ values for **3** are 0.66 at Cu3 and 0.60 at Cu8. The relation $\tau = (\beta - \alpha)/60°$, allows for an accurate distinction between trigonal-bipyramidal and square-pyramidal coordination geometries in pentacoordinated complexes {L5}M. β and α are the largest and second largest angles L−M−L′ ($\alpha < \beta \leq 180°$). A τ value equal to zero indicates an ideally square-pyramidal coordination sphere and τ = 1 is related to an ideal trigonal bipyramid: Addison, A. W.; Rao, T. N.; Reedijk, J.; van Rijn, J.; Verschoor, G. C. Synthesis, Structure, and Spectroscopic Properties of Copper(II) Compounds containing Nitrogen-Sulphur Donor Ligands; the Crystal and Molecular Structure of Aqua[l,7-bis(*N*-methylbenzimidazol-2'-yl)-2,6-dithiaheptane]copper(II) Perchlorate. *J. Chem. Soc., Dalton Trans.* **1984**, 1349−1356.
(41) Bera, M. K.; Pal, P.; Malik, S. Solid-state emissive organic chromophores: design, strategy and building blocks. *J. Mater. Chem. C* **2020**, *8*, 788−802.
(42) Remarkably, the available void space in the crystal lattice of **3**·$5Et_2O$ (4.6%, Figure S18) is similar to that of **2**·C_7H_8 (3.7%).
(43) Gómez, V.; Klyatskaya, S.; Fuhr, O.; Kalytchuk, S.; Zbořil, R.; Kappes, M.; Lebedkin, S.; Ruben, M. Pressure-Modulated Broadband Emission in 2D Layered Hybrid Perovskite-Like Bromoplumbate. *Inorg. Chem.* **2020**, *59*, 12431−12436.
(44) (a) *APEX2: Program for Data Collection on Area Detectors*; BRUKER AXS, Inc.: Madison, WI, 2010. (b) *APEX3: Program for Data Collection on Area Detectors*; BRUKER AXS, Inc.: Madison, WI, 2016.
(45) Sheldrick, G. M. *SADABS: Program for Absorption Correction of Area Detector Frames*; University of Göttingen: Göttingen, Germany, 2008.
(46) Sheldrick, G. M. *TWINABS: Program for Performing Absorption Corrections to X-Ray Diffraction Patterns Collected from Non-merohedrally Twinned and Multiple Crystals*; University of Göttingen: Göttingen, Germany, 2013.
(47) (a) Sheldrick, G. M. A short history of *SHELX*. *Acta Crystallogr.* **2008**, *A64*, 112−122. (b) Sheldrick, G. M. Crystal structure refinement with *SHELXL*. *Acta Crystallogr.* **2015**, *C71*, 3−8.
(48) Dolomanov, O. V.; Bourhis, L. J.; Gildea, R. J.; Howard, J. A. K.; Puschmann, H. *OLEX2*: a complete structure solution, refinement and analysis program. *J. Appl. Crystallogr.* **2009**, *42*, 339−341.
(49) (a) Spek, A. L. *PLATON: A Multipurpose Crystallographic Tool*; Utrecht University: Utrecht, The Netherlands, 2008; . (b) Spek, A. L. Single-crystal structure validation with the program *PLATON*. *J. Appl. Crystallogr.* **2003**, *36*, 7−13.
(50) (a) Perdew, J. P.; Burke, K.; Ernzerhof, M. Generalized Gradient Approximation Made Simple. *Phys. Rev. Lett.* **1996**, *77*, 3865−3868. (b) Adamo, C.; Barone, V. Toward reliable density functional methods without adjustable parameters: The PBE0 model. *J. Chem. Phys.* **1999**, *110*, 6158−6170. (c) Ernzerhof, M.; Scuseria, G. E. Assessment of the Perdew-Burke-Ernzerhof exchange-correlation functional. *J. Chem. Phys.* **1999**, *110*, 5029−5036.
(51) (a) Jesser, A.; Rohrmüller, M.; Schmidt, W. G.; Herres-Pawlis, S. Geometrical and Optical Benchmarking of Copper Guanidine−Quinoline Complexes: Insights from TD-DFT and Many-Body Perturbation Theory. *J. Comput. Chem.* **2014**, *35*, 1−17. (b) Hoffmann, A.; Rohrmüller, M.; Jesser, A.; dos Santos Vieira, I.; Schmidt, W. G.; Herres-Pawlis, S. Geometrical and Optical Benchmarking of Copper(II) Guanidine−Quinoline Complexes: Insights from TD-DFT and Many-Body Perturbation Theory (Part II). *J. Comput. Chem.* **2014**, *35*, 2146−2161. (c) Hoffmann, A.; Rohrmüller, M.; Jesser, A.; dos Santos Vieira, I.; Schmidt, W. G.; Herres-Pawlis, S. Corrigendum: Geometrical and Optical Benchmarking of Copper(II) guanidine−quinoline complexes: Insights from TD-DFT and Many-Body Perturbation Theory (Part II). *J. Comput. Chem.* **2015**, *36*, 272. (d) Xu, S.; Gozem, S.; Krylov, A. I.; Christopher, C. R.; Weber, J. M. Ligand influence on the electronic spectra of monocationic copper-bipyridine complexes. *Phys. Chem. Chem. Phys.* **2015**, *17*, 31938−31946. (e) Dereli, B.; Ortuño, M. A.; Cramer, C. J. Accurate Ionization Energies for Mononuclear Copper Complexes Remain a Challenge for Density Functional Theory. *ChemPhysChem* **2018**, *19*, 959−966.
(52) Martin, R. L. Natural transition orbitals. *J. Chem. Phys.* **2003**, *118*, 4775−4777.

https://doi.org/10.1021/acs.inorgchem.4c01646
Inorg. Chem. 2024, 63, 12943−12957